Bull Volcanol (2009) 71:1091–1110
DOI 10.1007/s00445-009-0296-4

RESEARCH ARTICLE

Continuing inflation at Three Sisters volcanic center, central Oregon Cascade Range, USA, from GPS, leveling, and InSAR observations

Daniel Dzurisin · Michael Lisowski · Charles W. Wicks

Received: 28 November 2007 / Accepted: 24 April 2009 / Published online: 17 June 2009

Abstract Uplift of a broad area centered ~6 km west of the summit of South Sister volcano started in September 1997 (onset estimated from model discussed in this paper) and was continuing when surveyed in August 2006. Surface displacements were measured whenever possible since August 1992 with satellite radar interferometry (InSAR), annually since August 2001 with GPS and leveling surveys, and with continuous GPS since May 2001. The average maximum displacement rate from InSAR decreased from 3–5 cm/yr during 1998–2001 to ~1.4 cm/yr during 2004–2006. The other datasets show a similar pattern, i.e., surface uplift and extension rates decreased over time but deformation continued through August 2006. Our best-fit model to the deformation data is a vertical, prolate, spheroidal point-pressure source located 4.9–5.4 km below the surface. The source inflation rate decreased exponentially during 2001–2006 with a 1/*e* decay time of 5.3 ± 1.1 years. The net increase in source volume from September 1997 to August 2006 was 36.5–41.9 x 10^6 m^3. A swarm of ~300 small ($M_{\max}=1.9$) earthquakes occurred beneath the deforming area in March 2004; no other unusual seismicity has been noted. Similar deformation episodes in the past probably would have gone unnoticed if, as we suspect, most are small intrusions that do not culminate in eruptions.

Keywords Three Sisters · South Sister · Cascade Range · Volcanology · Geodesy · Radar interferometry · InSAR · GPS · Leveling · Deformation · Uplift

Background

Three Sisters in the central Oregon Cascade Range is a long-lived center of basaltic to rhyolitic volcanism that includes three large composite cones of Quaternary age: Middle Sister, South Sister, and Broken Top. Most, if not all, of Middle and South Sisters is of late Pleistocene age (Calvert et al. 2003; Fierstein et al. 2003). South Sister's most recent eruptions occurred in two closely spaced episodes between 2.2 ka and 2.0 ka, producing rhyolite tephra, pyroclastic flows, lava flows, and lava domes from vents on the volcano's south, southeast, east, and north flanks (Scott 1987). As recently as 1.6 to 1.2 ka, dominantly effusive eruptions of basaltic and andesitic lavas immediately north of Three Sisters built large shield volcanoes (e.g., Belknap Crater) and isolated cinder cones and lava flows (e.g., Collier Cone) (Scott et al. 2001; Sherrod et al. 2004).

The discovery in April 2001 of crustal uplift centered near South Sister, which was recognized from time-sequential radar interferograms to have started sometime during 1996–1998, prompted increased seismic, geodetic, and geochemical monitoring of the area. This paper reports results of ongoing geodetic studies including radar interferometry, annual GPS and leveling surveys, and continuous

Editorial responsibility: J. Stix

D. Dzurisin (✉) · M. Lisowski
David A. Johnston Cascades Volcano Observatory,
U.S. Geological Survey,
1300 S.E. Cardinal Court, Building 10, Suite 100,
Vancouver, WA 98683-9589, USA
e-mail: dzurisin@usgs.gov

C. W. Wicks
U.S. Geological Survey,
345 Middlefield Road, MS 977,
Menlo Park, CA 94025, USA

GPS observations through 2006. It updates earlier reports through 2000 and 2003 (Wicks et al. 2002; Dzurisin et al. 2005) and presents new modeling results that improve on previous efforts.

Uplift at Three Sisters was discovered by Wicks et al. (2002), who produced several interferograms from radar images acquired during 1992–2000 by the European Space Agency's (ESA) ERS-1 and ERS-2 satellites. The interferograms showed progressive uplift of a ~10 x 20 km area centered ~5 km west of the summit of South Sister, starting sometime between August 1996 and September 1998. Wicks et al. (2002) modeled the source as a point pressure source (Mogi 1958) 6.5±0.4 km deep with a volume increase through September 2000 of 23 ± 3 x 10^6m^3, corresponding to an average inflation rate of 5.8 x 10^6m^3/yr if the onset of inflation was August 1996 (11.5 x 10^6m^3/yr if September 1998). They attributed the uplift to an ongoing episode of magma intrusion.

Dzurisin et al. (2005) reported results from: (1) additional radar interferograms through 2001 (no useful interferograms were obtained for 2002 or 2003); (2) tilt-leveling surveys at South Sister in 1985, 1986, and 2001; (3) electro-optical distance meter (EDM) surveys at South Sister in 1985 and 1986 compared to a GPS survey in 2001; (4) campaign GPS observations in 2001, 2002, and 2003 of a network of bench marks spanning the deforming area; (5) continuous GPS (CGPS) stations HUSB and PMAR, established in May 2001 and April 2002, respectively (station WIFC was added in July 2004); and (6) leveling surveys in 2002 and 2003 along two lines that intersect near the deformation center. They simultaneously inverted the radar interferometry (InSAR), GPS, and leveling data using a point pressure source (Mogi 1958), an ellipsoidal source (Yang et al. 1988; Fialko and Simons 2000; Fialko et al. 2001), and a dislocation source (dike or sill) (Okada 1985; Feigl and Dupré 1999). The best fit was produced by a shallowly dipping sill centered at 6.5 ± 2.5 km depth and inflating at an average rate of 5.0 ± 1.5 x 10^6m^3/yr, which Dzurisin et al. (2005) interpreted as magmatic intrusion along the brittle-ductile interface.

In this paper we report GPS, leveling, and InSAR results for the Three Sisters area through 2006, which show that the inflation rate decreased exponentially during 1997–2006. Using the same datasets through 2003, Dzurisin et al. (2005) assumed that the inflation rate was constant from 1995 to 2003. We show here that this assumption skewed the earlier analysis toward an incorrect dipping sill model. Our analysis of longer time-series datasets shows that a vertical, prolate spheroid source with time-invariant location and shape, but an exponentially decreasing inflation rate, provides the best fit to all of the deformation datasets for the entire inflation episode through August 2006.

Geodetic data, 2001–2006

SAR interferometry (InSAR)

Interferograms produced from images acquired by ERS-1 and ERS-2 from 1992 to 2001 were discussed by Wicks et al. (2002) and Dzurisin et al. (2005). Useful interferograms were obtained only with autumn-to-autumn image pairs, for two reasons: (1) enduring winter snow cover in the area (typically October–July) causes rapid loss of coherence, and (2) the surface deformation rate was too low (few cm/yr) to be measured reliably over shorter intervals, given the resolution of the InSAR technique (2.83 cm/fringe at C-band) and the orbit repeat intervals of operational SAR satellites (24–46 days).

Our attempts to make useful interferograms for 2002–2003 from ERS images were unsuccessful. For 2004–2006, we used images acquired by Envisat, the European Space Agency's follow-on to the ERS satellites, to produce two interferograms presented here. Each spans a 735-day interval, shifted 4 days with respect to the other, from September 2004 to October 2006. One is from descending track 385 and the other is from ascending track 435 (Table 1, Figs. 1 and 2). We were not able to produce a useful interferogram for 2005–2006, nor for any interval shorter than about one year. Except under very special circumstances, ERS and Envisat images cannot be combined to produce interferograms owing to technical differences between the radars, so there are no interferograms that span, for example, 2001–2004.

Despite some minor differences, both of the 2004–2006 interferograms show a similar pattern of ground deformation centered a few kilometers west of the summit of South Sister. Maximum range change is nearly one fringe (28.3 mm for Envisat) in both cases. The average maximum range change for 2004–2006 (~0.5 fringe/yr or ~1.4 cm/yr) is about half the rate reported by Wicks et al. (2002) for 1996–2000 and by Dzurisin et al. (2005) for 2000–2001 (~1 fringe/yr in both cases). The Three Sisters area is located at far range in images acquired on track 435, so special processing of the raw backscatter data is required to produce a focused SAR image centered in that area. This results in lower signal-to-noise and weaker coherence at extreme far range, which is apparent in the eastern third of Fig. 2 where coherence is lost entirely (see "Methods", item 1). Coherence is also lost in the western part of the interferogram owing to dense forest cover. Small atmospheric phase-delay anomalies are likely present and can account for subtle differences between the 2004–2006 interferograms. One obvious difference, an east-west shift in the location of maximum range change, results from the different viewing geometries for ascending and descending tracks (see "Methods", item 2). We accounted for this effect in the models discussed below.

Table 1 Parameters for interferograms discussed in text. Satellite unit look vector is positive in the direction (East, North, Up). For information about the Advanced Synthetic Aperture Radar (ASAR) aboard Envisat, see http://www.eurimage.com/products/envisat.html and http://envisat.esa.int/object/index.cfm?fobjectid=3772

Mode–Track	Image 1 Date	Image 2 Date	Interval (days)	Baseline (m)	Satellite Unit Look Vector
IS2–T385 (descending)	26 Sept. 2004	01 Oct. 2006	735	91	(0.34, −0.08, 0.94)
IS2–T435 (ascending)	30 Sept. 2004	05 Oct. 2006	735	107	(−0.45, −0.09, 0.89)

“Baseline” refers to the horizontal separation between vantage points for two overlapping SAR images, measured perpendicular to the SAR trajectories. To preserve the interferometric effect, the baseline distance must be less than ~1 km. Image pairs with long baselines are sensitive to topography and therefore are a good choice if the goal is to produce a digital elevation model (DEM). Shorter baselines are preferable if the goal is to measure ground deformation, because the sensitivity to topographic errors is correspondingly lower.

In Fig. 3, we compare vertical surface displacements from August 2004 to August 2006, as measured by InSAR and leveling, along two level lines that intersect near the deformation center (see “Methods”, item 3). Relative height changes measured by leveling were converted to absolute vertical displacements using the best-fit model discussed below. The zero-change datum for the interferograms was taken to be the average of several points that are distant from the deformation center and where coherence is good in both interferograms. Maximum uplift measured by the two techniques is similar: 19.8 ± 3.7 mm at bench mark **5** from leveling and 26.8 ± 10 mm at **6** from InSAR. Stated uncertainty in the leveling observation includes the effects of random leveling error, benchmark instability, and uncertainty in our best-fit model (see **Leveling Surveys**). Uncertainty in the InSAR measurement is estimated from experience with numerous C-band interferograms and is otherwise unconstrained.

Continuous GPS (CGPS) observations

To continuously track deformation in the Three Sisters area, the U.S. Geological Survey (USGS), working in coopera-

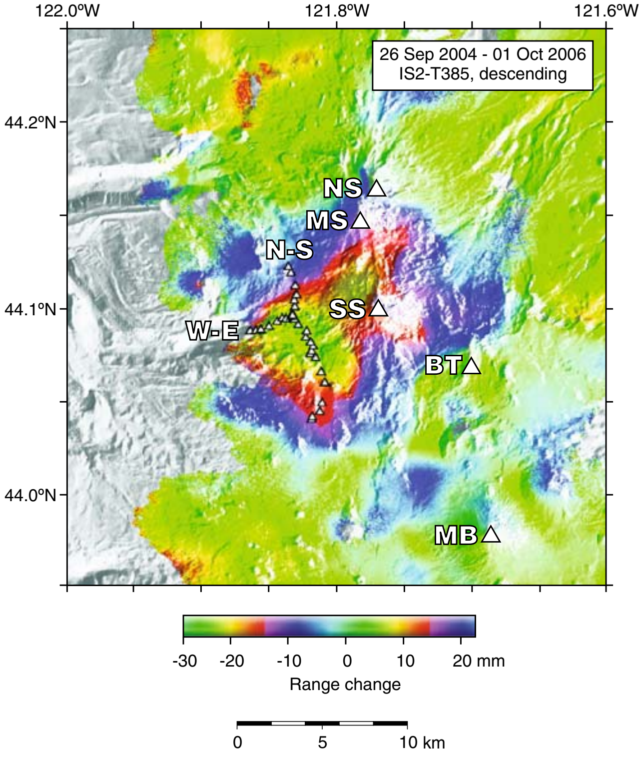

Fig. 1 Interferogram of the Three Sisters area, draped over topography, for 26 September 2004–01 October 2006 from Envisat images acquired along descending track 385 (Table 1). NS, North Sister; MS, Middle Sister; SS, South Sister; BT, Broken top; MB, Mount Bachelor; N-S, north end of north-south level line; W-E, west end of west-east level line; triangles, bench marks along level lines

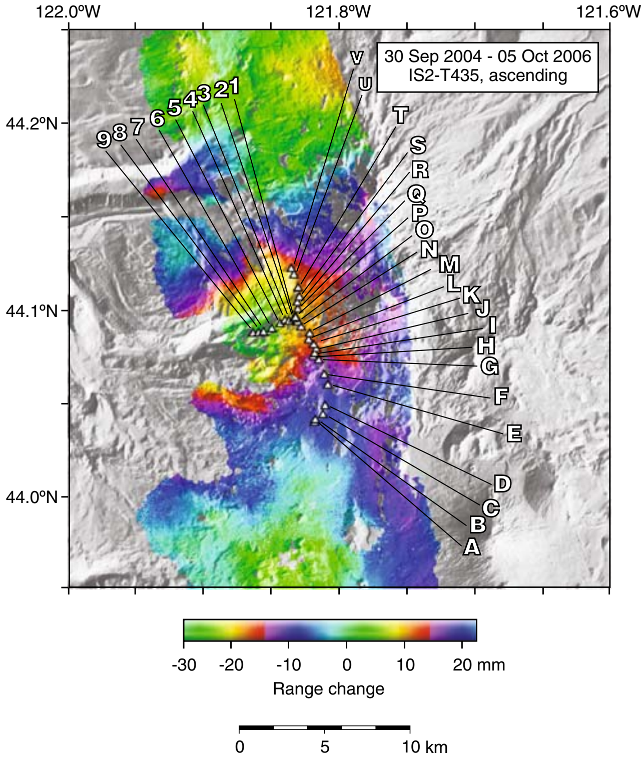

Fig. 2 Interferogram of the Three Sisters area, draped over topography, for 30 September 2004–05 October 2006 from Envisat images acquired along ascending track 435 (Table **1**). Symbols as in Fig. 1. Labels **V**–**A** and **9**–**1** represent bench marks along N–S and W–E level lines, respectively

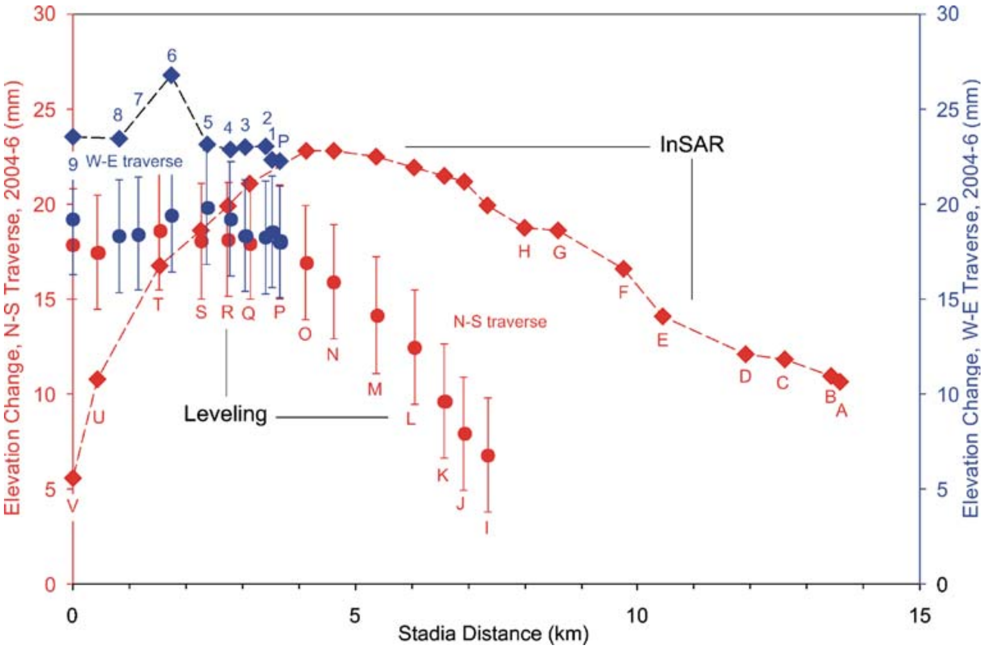

Fig. 3 Profiles of elevation change from InSAR (diamonds) and leveling (circles, 1 standard deviation error bars) along two level lines for August 2004–August 2006. Red, N–S line; blue, W–E line. Lines intersect at **P**. Elevation changes were calculated from range changes measured along Envisat ascending track 435 and descending track 385 ("Methods", item 3). Both InSAR and leveling profiles show greatest uplift near **O**, consistent with our best-fit model derived from leveling and GPS observations. See Fig. 2 for mark locations and text for discussion

tion with the U.S. Forest Service (USFS), installed three CGPS stations during 2001–2004. HUSB, located ~2 km northwest of the deformation center, was installed near The Husband in May 2001. PMAR at Pine Marten Lodge on the north flank of Mount Bachelor was added in April 2002. The station is located ~15 km southeast of the deformation center, near the southeast margin of the deformation field delineated by InSAR. The third station, WIFC, was installed near The Wife, ~4 km southeast of the deformation center, in July 2004 (Fig. 4). All three CGPS stations are subject to ice and snow accumulation in winter, and WIFC was damaged by snow creep in winter 2005. We did not attempt to analyze the small amount of useful data recorded at WIFC before the station was damaged.

GPS data were processed with GIPSY/OASIS II software using the point-positioning method (Zumberge et al. 1997)), following procedures outlined by Savage et al. (2001a). We computed station positions in the ITRF2000 reference frame and transformed them into a nominally stable North American Plate reference frame. About 50 global stations with well-determined velocities were included in the solution. Using QOCA (Dong et al. 1998), the daily solutions were translated into a local reference frame defined by a subset of CGPS stations that are outside the volcanically deforming area and that have well-determined positions and velocities. QOCA applies a Helmet transformation to the loosely constrained daily solutions for stations in the local network to produce solutions in which the positions of the local reference stations are most consistent with their projected values. No position constraints were applied to stations in the volcanically deforming area near Three Sisters. This operation removes a common-mode daily bias in the solutions (equivalent to small local network translations), and it can reduce scatter in station-component time series by a factor of 2 to 3 (Williams et al. 2004).

Previous geodetic studies of the Cascadia margin (Svarc et al. 2002; McCaffrey et al. 2000, 2007) revealed that the Three Sisters region is undergoing steady rigid-body rotation about a pole located near the eastern boundary of Oregon. The more detailed studies by McCaffrey et al. (2007) divided Oregon into several blocks separated by bounding faults. To reveal the volcanic deformation near Three Sisters, we estimated and removed the background tectonic motion using the method described by Savage et al. (2001a, b) to compute a best-fitting Euler pole, rotation rate, and residual strain (Table 2). We modeled velocities from 17 campaign GPS stations located in eastern Oregon outside of the Three Sisters area, along with those from the Pacific Northwest Geodetic Array (PANGA) CGPS stations REDM (east of Three Sisters) and GOBS (northeast). Our results are comparable to the m05G model, block OrID results of McCaffrey et al. (2007).

The daily displacement component time series from station HUSB (Fig. 5), corrected for predicted background horizontal tectonic motion, indicate that the rate of inflation has decayed progressively since station HUSB was installed in May 2001. Decaying displacements also were observed at station PMAR. We applied the maximum likelihood estimator (MLE; Langbein 2004) to model the station displacement component time series as the sum of a mean value, a linear rate (steady tectonic background deformation), annual and semi-annual perturbations (sea-

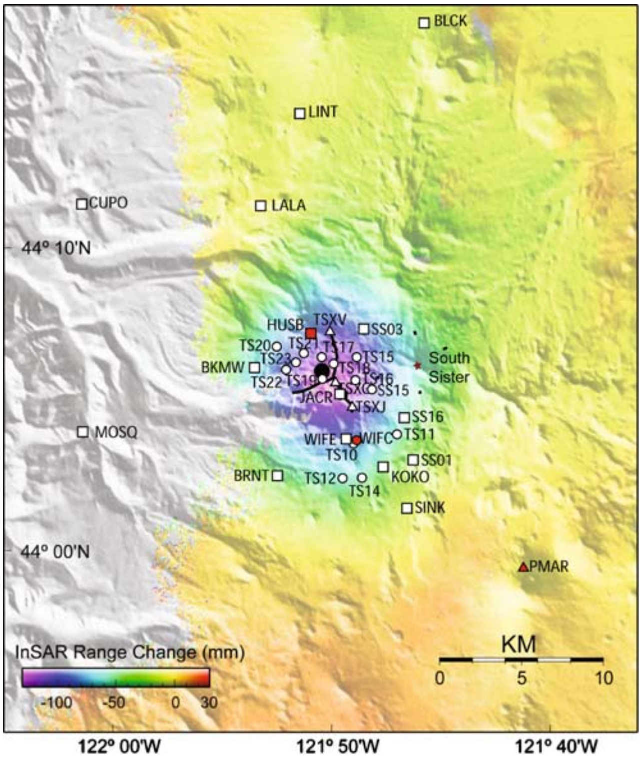

Fig. 4 Map of CGPS (red) and campaign GPS (white) stations on a background of gray shaded relief and colored InSAR total range change from August 1995 to August 2001. Stations shown as squares were first surveyed in 2001, those shown as triangles were added in 2002, and those shown as circles were added in 2003 or 2004. Thick black line marks the level lines and large black circle the center of uplift as determined from the GPS and level surveys. Four tilt-leveling stations are shown as stubby black lines (dashes) on the flanks of South Sister, surrounding the volcano's summit (red star). See text ("Modeling Results") for details

sonal noise), and exponentially decaying deformation (volcanic deformation):

$$d_i = D_0 + R(t_i - t_0) + S\ \sin(2\pi f((t_i - t_0) + \phi)) + ae^{-b(t_i - t_0)} \tag{1}$$

where t_0 is the time that the deformation episode began, the observation d_i is made at time t_i, and D_0, R, S, φ, a, and b are constants to be determined ($b=1/\tau$, where τ is the $1/e$ decay time in years).

CGPS data are affected by both random and temporally correlated noise (white noise, WN, and colored noise, CN, respectively). The regression for rate and decay parameters must account for WN and, at minimum, two types of CN: flicker (FL) and random walk (RW) noise (Langbein 2008). Our MLE regression allowed the noise model to vary along with the rate and decay parameters.

The high mountain locations of stations HUSB (2,038 m) and PMAR (2,348 m) expose them to severe weather that can bury the GPS antennas in snow or coat them with rime, which shifts the antenna phase center and produces pseudo-offsets in the displacement time series. As part of the regression, we identified and removed as outliers those station displacements with either a horizontal component residual greater than 5 mm or a vertical component residual greater than 15 mm. A total of 146 (8%) of 1869 HUSB and 289 (17%) of 1706 PMAR daily observations were identified as outliers. Nearly all of the outliers occurred during winter.

In our initial unconstrained MLE regression of Eq. 1, we found that the slowly decaying CGPS displacements were best fit by background rates much higher than those predicted by the tectonic model. This result is unreasonable, so we constrained the decay rate for volcanic deformation to be longer than 1.5 years. Then we constrained the background rate, R, to that predicted by the tectonic model and assumed that displacement components (East, North, Up) at stations HUSB and PMAR decayed at the same rate. The MLE regression was run iteratively through a range of decay rates (b) to estimate the exponential coefficient (a) and the WN (mm), FL (mm/yr$^{0.25}$), and RW (mm/yr$^{0.5}$) noise components. The resulting MLEs (misfits) were summed for each value of b and the minimum summed MLE, with its corresponding noise model, was chosen to be the best-fitting decay rate (Table 3). With these constraints, the $1/e$ decay time for the Three Sisters deformation episode is 5.3 ± 1.1 years at 95% confidence.

Wicks et al. (2002) concluded from InSAR observations that the Three Sisters deformation episode began sometime between August 1996 and September 1998. However, for our time series analysis we used a start time of May 2001, the date when station HUSB was installed. Later in this

Table 2 Best-fit Euler vectors and uniform strains based on campaign GPS and continuous GPS data from this study (column 4), compared to results of earlier studies (columns 2 and 3)

Parameter	Svarc et al. (2002)	McCaffrey et al. (2007)	This Study
Latitude of pole, °N	43.40±0.14	45.99±0.20	44.62±0.14
Longitude of pole, °W	119.33±0.28	115.46±0.20	116.49±0.68
Angular Velocity, deg Myr^{-1}	−0.822±0.057	−0.406±0.021	−0.547±0.078
ε_{EE} , nstrain yr^{-1}	−7.4±1.8		−8.6±2.4
ε_{EN} , nstrain yr^{-1}	−3.4±1.0		0.1±1.4
ε_{NN} , nstrain yr^{-1}	−5.0±0.8		−4.7±1.4
Normalized variance	1.6		0.9

Values for the McCaffrey et al. (2007) study are for model m05G, block OrId.

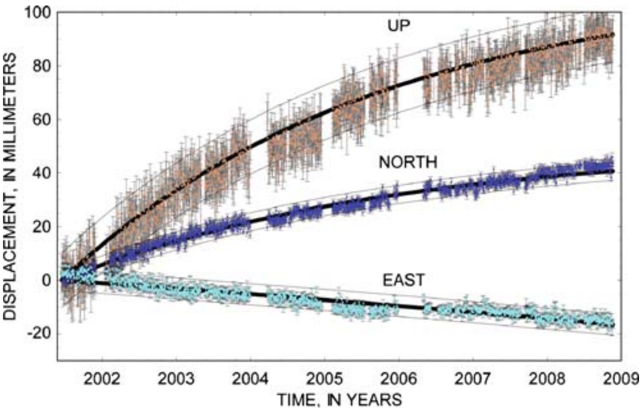

Fig. 5 Time series of HUSB displacement components. Data are corrected for steady tectonic background movement and seasonal perturbations. Error bars represent ± 1 standard deviation. Thick solid line is best-fitting rate of exponential decay and thin solid lines are 95% confidence limits of this fit (see Table 1)

paper, we apply the decay rate derived from the analysis of HUSB and PMAR CGPS data to estimate when the episode began and the projected source volume change.

Campaign GPS observations

Dzurisin et al. (2005) described the campaign GPS network at Three Sisters and reported results for 2001–2003. Thirteen new stations were added in 2003, and almost all stations were surveyed with similar equipment and procedures in 2004, 2005, and 2006 (Fig. 4). GPS station velocities and modeling results through 2003 reported by Dzurisin et al. (2005) assumed that the deformation rate was constant with time. However, our time-series analysis of the displacement of CGPS stations HUSB and PMAR shows instead that the deformation rate decayed predictably with time. The spatial pattern of time-dependent deformation was estimated by assuming an exponential decay rate and calculating the exponential coefficient that best-fits the campaign GPS station displacement components through time.

In the campaign GPS time-series analysis, we corrected observed horizontal displacements for background deformation predicted by our tectonic model (Table 2), set the start time t_0 to 2001.4 (May 2001), and constrained the decay time b=1/5.3 year^{-1} to that derived from the CGPS data. We assumed no accumulating background vertical displacements. The campaign GPS observations were made at roughly the same time each year (August–September), so annual and semi-annual terms in Eq. 1 were ignored. A noise model was prescribed because of the small number of surveys. The fixed WN, FL, and RW noise components were scaled up from the values obtained from the CGPS analysis, with the horizontal displacement component noise computed using WN=3 mm, FL=6 mm year$^{-0.25}$, and

Table 3 Exponential fits to CGPS station displacements. Shown are best-fit constant coefficients for $y = R(t_i - t_0) + S\,\sin(2\pi f((t_i - t_0) + \phi)) + ae^{-b(t_i - t_0)}$ with t_0=2001.4 (May 2001) (Eq. 1 minus time-invariant term D_0)

Component	a (mm)	1/b (yr^{-1})	R (fixed) (mm·yr^{-1})	White Noise (mm)	Flicker Noise (mm·yr$^{-0.25}$)	Random Walk Noise (mm·year$^{-0.5}$)	Annual Amplitude (mm)	Annual Phase (degree)	Semi-annual Amplitude (mm)	Semi-annual Phase (degree)
HUSB East	−23.8±1.2	5.3	−0.1	1.2±0.1	3.0±0.2	0.0±0.4	1.5±0.1	351±5	0.5±0.1	142±15
HUSB North	55.4±2.8	5.3	3.9	1.1±0.1	2.8±0.2	0.7±0.4	0.6±0.1	181±14	0.0±0.1	234±360
HUSB Up	121.0±3.6	5.3	0.0	4.3±0.1	8.7±0.8	0.0±0.1	4.0±0.4	121±5	1.2±0.4	44±16
PMAR East	23.9±4.0	5.3	−0.3	1.3±0.1	3.4±0.3	0.9±0.4	1.7±0.1	232±4	0.5±0.1	21±14
PMAR North	−18.6±2.1	5.3	3.9	1.2±0.1	4.0±0.3	0.0±0.1	0.3±0.1	215±26	0.5±0.1	35±15
PMAR Up	−16.7±7.7	5.3	0.0	4.0±0.1	15.1±0.8	0.0±0.8	2.9±0.4	196±7	0.6±0.4	207±37

R is fixed to the linear rate of tectonic background motion given by the tectonic model, *a* and *b* are magnitude and 1/*e* decay constant for the exponentially decaying component of motion. Also shown are white, flicker, and random walk noise estimates and the magnitudes and phases of seasonal (annual and semiannual) perturbations, all with one standard deviation uncertainties.

RW=2 mm year$^{-0.5}$, and vertical component noise computed using WN=10 mm, FL=12 mm year$^{-0.25}$, and RW=3 mm year$^{-0.5}$. When the RMS scatter from the exponential fit exceeded the predictions of the noise model, we allowed the WN component to increase until the scatter matched the noise model. Best-fitting exponential coefficients and their 1 standard deviation uncertainties are given in Table 4. The horizontal coefficients and their estimated 95% confidence error ellipses are plotted as vectors in Fig. 6a, and the vertical coefficients and their 95% confidence error bars are plotted in Fig. 6b. Horizontal displacement vectors radiate outward from a point ~6 km west of the summit of South Sister, where vertical displacements are largest.

Leveling surveys

Level lines along two USFS trails that intersect near the James Creek shelter, within 2 km of the deformation center, were established in September 2002 and measured each August or September from 2002 to 2006. Previously, four tilt-leveling lines, each 200–320 m long, had been established on the flanks of South Sister in 1985 and remeasured in 1986 and 2001 (Dzurisin et al. 2005). They are difficult to access with leveling equipment and not well situated to track the broad deformation field that began developing to the west in 1996–1998. For that purpose, we established longer lines along trails closer to the deformation center. The north-south line along James Creek Trail 3546 is 13.6 km long (stadia distance) and comprises bench marks **V**–**A**; **O** is at the shelter. Marks **V**–**I** were observed in 2002 and 2004; **V**–**J** in 2003, and **V**–**A** in 2005 and 2006. The west-east line along Separation Creek Trail 3524 is 3.2 km long and comprises marks **9**–**1** plus **P**, where it intersects the north-south line (Fig. 2). The entire line was observed each August or September from 2002 to 2006. Elevation differences between marks on both lines, with average spacing of 560 m (1460 m maximum), were measured by differential leveling using a Leica NA3003 digital level and calibrated barcode rods. Field procedures conformed in most respects to standards for first-order, class II leveling surveys established by the National Geodetic Survey (Federal Geodetic Control Committee 1984). A level collimation procedure was followed each survey day. Corrections for rod scale, temperature, and refraction were applied to field observations. Differential astronomic and orthometric corrections were not applied because they are negligible for lines this short (Balazs and Young 1982). See Dzurisin et al. (2005) for additional details.

Results from annual leveling surveys are consistent with a decaying deformation rate as shown by GPS observations, although the signal-to-noise ratio is considerably lower in the leveling data. Figure 7 shows year-to-year elevation changes along both lines from August 2002 to August 2006. We used the best-fit model described below ("Source Modeling Results") to calculate the absolute vertical displacement of **V** at epochs corresponding to the leveling surveys, and combined those results with the relative elevation changes measured by leveling to compute the absolute elevation change at each mark. From Fig. 7 we see that the greatest uplift occurred near the lines' intersection at **P**, which moved up 23.6 ± 3.5 mm, 18.6 ± 3.5 mm, 8.7 ± 3.5 mm, and 10.5 ± 3.5 mm during 2002–2003, 2003–2004, 2004–2005 and 2005–2006, respectively. The stated uncertainty is our best estimate of the combined effects of random leveling error, benchmark instability (random walk noise), and model uncertainty. For first-order leveling surveys, the first two error sources are approximated by:

$$\sigma = \sqrt{\left(1.0mm \cdot km^{-1/2} \cdot \sqrt{\Delta L}\right)^2 + \left(0.5mm \cdot yr^{-1/2} \cdot \sqrt{\Delta t}\right)^2} \tag{2}$$

where ΔL is stadia distance along the level line and Δt is time between surveys (Vanicek et al. 1980; Wyatt 1989). The coefficient of the second term ($0.5 mm{\cdot}yr^{-1/2}$ in this case) depends on the quality of the bench mark. For geodetic marks set in bedrock or on deeply anchored rods, it is generally in the range 0.2–$1.0 mm{\cdot}yr^{-1/2}$ (Wyatt 1989). All of the marks used for leveling at Three Sisters are stainless steel pins 10 cm long and 1.3 cm in diameter, set with epoxy in holes drilled into bedrock or large buried boulders. Our choice of $0.5 mm{\cdot}yr^{-1/2}$ is thought to be appropriate for this type of mark, and is consistent with the noise model derived below ("Source Modeling Results"). Using ΔL=3.7 km (stadia distance from **V** to **P**) and Δt=1 yr in Eq. 2 gives σ =2.0 mm. Based on the average misfit between our best-fit model, leveling observations, and CGPS-derived elevations at HUSB and PMAR, we estimated the uncertainty arising from our use of the model to calculate the elevation at **P** as a function of time to be 2 mm, or $2 \cdot \sqrt{2}$ mm=2.8 mm for the change in elevation at **P** between any two leveling surveys. So our estimate of the total uncertainty in absolute elevation changes at **P** measured by sequential annual leveling surveys is $\sqrt{(2.0mm)^2 + (2 \cdot \sqrt{2}mm)^2} = 3.4$ mm.

Note from Fig. 7 that any difference in uplift rate between 2004–2005 and 2005–2006 is poorly determined by the leveling data. On the other hand, the uplift rate was clearly greatest in 2002–2003, slowed somewhat during 2003–2004, and slowed considerably thereafter. This trend is generally consistent with the exponentially decreasing rate of motion seen at HUSB (Fig. 5). There is a suggestion in Fig. 7 that the location of maximum uplift shifted slightly northward and westward (i.e., toward **V** and **9**) during 2004–2006 relative to 2002–2004, but the difference is small compared to uncertainty in the leveling observations

Table 4 Amplitude of exponential term in Eq. 1 (North, East, and Up components) estimated from campaign GPS and leveling data. Annual GPS surveys comprising at least two consecutive days of observations were made at most stations, with a few exceptions

Station	Latitude (°N)	Longitude (°E)	Elevation (m)	North Amplitude and Standard deviation, σ_N (mm)	East Amplitude and Standard deviation σ_E (mm)	Vertical Amplitude and Standard deviation σ_{UP} (mm)	Date of Initial Measurement
BKMW	44.1010	−121.8920	1696	13.3±9.1	−78.7±9.1	101.4±18.0	2001.7 (August 2001)
BRNT	44.0410	−121.8740	1908	−71.4±8.9	−25.1±8.9	43.9±16.3	2001.7 (August 2001)
CUPO	44.1910	−122.0240	969	11.8±9.3	−18.2±9.3	−20.8±19.3	1999.7 (August 1999)
HUSB	44.1200	−121.8490	2039	55.6±4.0	−25.3±4.0	121.0±3.6	2001.4 (May 2001)
JACR	44.0850	−121.8270	1791	−31.9±8.9	27.0±8.9	111.5±18.0	2001.7 (August 2001)
KOKO	44.0463	−121.7945	1838	−49.2±9.5	33.7±9.7	25.1±20.3	2001.7 (August 2001)
LALA	44.1890	−121.8870	1372	28.2±9.4	−12.9±10.2	[−113.2±23.2]	2001.6 (July 2001)
MOSQ	44.0646	−121.0236	1014	−3.5±9.2	−17.6±10.2	−18.3±23.0	2001.6 (July 2001)
PMAR	43.9910	−121.6870	2349	−18.7±5.1	21.7±5.1	−16.7±8.7	2002.4 (May 2002)
SINK	44.0230	−121.7760	1647	−32.1±10.5	31.4±9.8	−14.7±22.8	2001.6 (July 2001)
SS01	44.0490	−121.7710	2045	−39.3±9.2	45.5±9.2	24.3±18.3	2001.7 (August 2001)
SS03	44.1210	−121.8090	2039	30.8±9.2	41.3±9.2	111.5±18.3	2001.7 (August 2001)
SS15	44.0880	−121.8030	2184	−11.8±9.3	58.1±9.1	78.6±19.5	2001.7 (August 2001)
SS16	44.0730	−121.7770	2107	−25.7±11.0	60.7±11.0	31.3±21.9	2001.7 (August 2001)
TS10	44.0590	−121.8170	1928	−57.1±14.0	57.9±14.0	100.9±29.3	2003.7 (August 2003)
TS11	44.0642	−121.7831	1933	−16.4±14.0	31.0±14.0	57.8±29.1	2003.7 (August 2003)
TS12	44.0445	−121.8286	1818	−92.2±19.8	25.4±19.8	61.9±46.1	2004.6 (July 2004)
TS14	44.0400	−121.8100	1828	−28.5±14.0	36.2±14.0	−23.8±28.8	2003.7 (August 2003)
TS15	44.1060	−121.8140	1901	1.6±14.0	67.7±14.0	92.1±31.3	2003.7 (August 2003)
TS16	44.0940	−121.8150	1895	−12.0±14.0	67.2±14.1	144.5±37.5	2003.7 (August 2003)
TS17	44.1060	−121.8400	1721	38.3±14.4	19.5±14.4	177.8±31.1	2003.7 (August 2003)
TS18	44.1030	−121.8310	1806	−17.8±14.9	15.3±14.7	111.3±33.1	2003.7 (August 2003)
TS19	44.0940	−121.8400	1733	−26.0±16.8	10.2±13.1	94.4±44.4	2003.7 (August 2003)
TS20	44.1120	−121.8750	1775	40.4±19.1	−79.8±19.3	53.9±34.3	2003.7 (August 2003)
TS21	44.1080	−121.8540	1798	45.6±14.3	−24.9±14.3	158.2±30.4	2003.7 (August 2003)
TS22	44.1000	−121.8680	1713	−23.0±13.8	−67.7±14.0	130.0±27.4	2003.7 (August 2003)
TS23	44.1020	−121.8600	1719	49.6±14.4	−48.9±14.4	189.4±45.1	2003.7 (August 2003)
TSXJ	44.0790	−121.8170	1721	−33.2±11.4	35.4±11.2	87.2±23.3	2003.7 (August 2002)
TSXO	44.0930	−121.8310	1769	−7.0±10.8	24.6±10.9	103.9±25.1	2003.7 (August 2002)
TSXV	44.1220	−121.8350	1845	44.9±11.1	4.4±11.1	65.9±22.5	2003.7 (August 2002)
WIFE	44.0610	−121.8220	2020	−57.2±9.3	27.5±9.3	53.0±20.8	2001.7 (August 2001)
Exponential amplitudes for selected level sections							
V – U	44.12150	−121.83520	1845	–	–	−6.6±2.8	2002.7 (August 2002)
U – T	44.11809	−121.83330	1844	–	–	−7.2±3.4	2002.7 (August 2002)
T – S	44.11120	−121.83020	1822	–	–	−8.0±3.1	2002.7 (August 2002)
S – R	44.10638	−121.82920	1811	–	–	−9.1±2.8	2002.7 (August 2002)
R – Q	44.10326	−121.83090	1805	–	–	−2.9±2.7	2002.7 (August 2002)
Q – P	44.09990	−121.83050	1772	–	–	−1.1±2.9	2002.7 (August 2002)
P – O	44.09584	−121.83210	1775	–	–	0.0±2.8	2002.7 (August 2002)
O – N	44.09298	−121.83060	1766	–	–	5.4±2.8	2002.7 (August 2002)
N – M	44.09031	−121.82810	1789	–	–	7.8±3.1	2002.7 (August 2002)
M – L	44.08680	−121.82180	1815	–	–	1.8±3.0	2002.7 (August 2002)
L – K	44.08346	−121.82250	1773	–	–	10.9±2.9	2002.7 (August 2002)
K – J	44.08083	−121.81880	1727	–	–	4.5±2.7	2002.7 (August 2002)
J – I	44.07879	−121.81690	1719	–	–	4.3±2.8	2002.7 (August 2002)

Table 4 (continued)

Station	Latitude (°N)	Longitude (°E)	Elevation (m)	North Amplitude and Standard deviation, σ_N (mm)	East Amplitude and Standard deviation σ_E (mm)	Vertical Amplitude and Standard deviation σ_{UP} (mm)	Date of Initial Measurement
I – H	44.07607	−121.81810	1728	–	–	–	2005.7 (August 2005)
H – G	44.07477	−121.81930	1776	–	–	–	2005.7 (August 2005)
G – F	44.07258	−121.81520	1829	–	–	–	2005.7 (August 2005)
F – E	44.06485	−121.81100	1827	–	–	–	2005.7 (August 2005)
E – D	44.05929	−121.80850	1856	–	–	–	2005.7 (August 2005)
D – C	44.04828	−121.81030	1869	–	–	–	2005.7 (August 2005)
C – B	44.04360	−121.81210	1843	–	–	–	2005.7 (August 2005)
B – A	44.04073	−121.81770	1825	–	–	–	2005.7 (August 2005)
A	44.03955	−121.81810	1820				
9 – 8	44.08688	−121.86340	1555	–	–	−5.4±2.7	2002.7 (August 2002)
8 – 7	44.08713	−121.85920	1585	–	–	−3.6±2.7	2002.7 (August 2002)
7 – 6	44.08766	−121.85550	1603	–	–	−4.3±2.9	2002.7 (August 2002)
6 – 5	44.08943	-121.84960	1622	–	–	−4.9±3.0	2002.7 (August 2002)
5 – 4	44.09196	−121.84340	1660	–	–	−2.2±2.8	2002.7 (August 2002)
4 – 3	44.09383	−121.83980	1724	–	–	0.9±2.6	2002.7 (August 2002)
3 – 2	44.09332	−121.83690	1724	–	–	0.3±2.7	2002.7 (August 2002)
2 – 1	44.09467	−121.83350	1749	–	–	−0.1±2.4	2002.7 (August 2002)
1 – P	44.09530	−121.83220	1761	–	–	0.4±2.4	2002.7 (August 2002)
P	44.09584	−121.83210	1775				

There was no network survey in 2007, but LALA and BRNT were occupied for several days. A single outlier at LALA [brackets, column 7] was not used in the source parameter inversion. For leveling sections in the second part of the table, the latitude, longitude, and elevation in each row correspond to the first mark in the section (column 1). Amplitude of exponential term is relative to 2001.4 (May 2001). Block rotation and regional strain were removed from horizontal components of GPS displacements using a tectonic model. No corrections were applied to vertical displacements. Uncertainties are 1 standard deviation. See text for details, and Figs. 2 and 4 for station locations.

and such a shift is not indicated by the other datasets. When the leveling data are plotted as yearly cumulative changes since 2002 (Fig. 8), the uplift trend is more apparent. Progressive uplift is more obvious in this format because the deformation signal is coherent and grows, while the errors are mostly random and cancel. Cumulative uplift at **P** since 2002 was 23.6. mm ± 3.4 mm, 42.2 mm ± 3.5 mm, 50.9 mm ± 3.5 mm, and 61.3 ± 3.5 mm in 2003, 2004, 2005, and 2006, respectively. Uncertainties were estimated as above, using Eq. 2 with Δt=1, 2, 3, and 4 yr for 2002–2003, 2002–2004, 2002–2005, and 2002–2006, respectively, and the uncertainty associated with the model = $2 \cdot \sqrt{2}$ mm. The shapes of the two elevation-change profiles are best seen in Fig. 9, which shows cumulative elevation changes for 2002–2006, the interval with the highest signal-to-noise ratio, at an expanded vertical scale. Greatest uplift occurred between marks **S** and **N** on the north-south line and between **6** and **P** on the west-east line. This indicates that the deformation center is located less than 1 km northwest of the James Creek shelter and ~6 km west of the summit of South Sister, which is consistent with the InSAR and GPS results, and with the best-fit model discussed below.

When the leveling observations are extended to the south end of the N–S line at **A**, a similar pattern emerges. Figure 10 shows the 2005–2006 elevation-change profiles for both lines in their entirety (recall that segment **I**–**A** of the north-south line was measured only in 2005 and 2006). The greatest uplift occurred at marks **5** and **P**, 1.4 km west and 0.3 km north of the shelter, respectively. Uplift at **A**, the farthest mark ~7 km south-southeast of the deformation center, was 0.5 ± 4.6 mm. The uncertainty at **A** for 2005–2006 was estimated as above, using Eq. 2 with ΔL=13.6 km (**V**–**A** stadia distance), Δt=1 yr, and the model uncertainty = $2 \cdot \sqrt{2}$ mm. We conclude that the vertical deformation field is mostly inboard of **A**; elsewhere, the level lines do not extend far enough to estimate the boundary of the deformation field. Interferograms that collectively span 1992–2001 show it to be 10–20 km across (Wicks et al. 2002; Dzurisin et al. 2005), which is consistent with the 2005–2006 leveling results.

To facilitate modeling of the leveling data together with the GPS data, we estimated a best-fit exponential coefficient in Eq. 1 for elevation change in each level section, fixing the decay time to b=1/5.3 year^{-1} and ignoring seasonal perturbations. As with the GPS data, we assumed

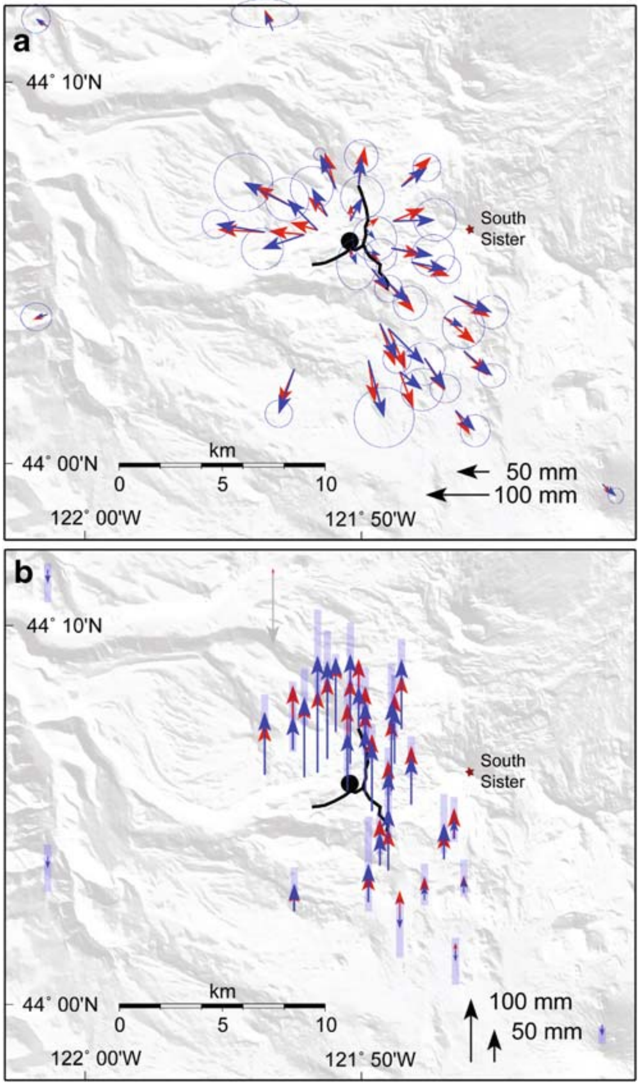

Fig. 6 Post-May 2001 campaign GPS and CGPS horizontal (A) and vertical (B) station displacements (blue vectors) predicted by the exponential fit to station displacement time series (see Table 4). Background tectonic deformation was modeled and removed before calculating exponential coefficients. Error ellipses (A) and shaded blue bars (B) represent 95% confidence limits for the tip of the vectors. Red arrows represent deformation predicted by the best-fitting vertical prolate spheroid source model (see Table **5**)

no background vertical displacements. The noise model used to weight a measured section elevation change is that given by Eq. 2. The exponential coefficients from the MLE regression are given in Table 4.

Source modeling results

We used the exponential coefficients of the GPS displacement components and leveling section elevation changes (Table 4) to estimate the location and cavity volume change of a buried pressure source. We made no attempt to characterize time-dependent range change in the interferograms, for two reasons. First, the number of interferograms is small and the intervals they span are discontinuous, which makes multiple-interferogram time series analysis difficult (Berardino et al. 2002). Second, the poorly known structure of temporally and spatially correlated noise in interferograms makes it difficult to properly weight InSAR data relative to other types of data for simultaneous inversions (Jónsson et al. 2002; Simons et al. 2002; Lohman and Simons 2005) (see “Methods”, item 4). Using the GPS and leveling data, we investigated a range of spheroidal cavity geometries and found that spherical and prolate (i.e., vertically elongate) point pressure sources fit the data better than sill-like cavities (Table 5). This is contrary to results reported by Dzurisin et al. (2005), who concluded that a sill-like cavity provided the best fit to their combined InSAR, GPS, and leveling data. However, we are convinced by our more recent analysis that a spherical or prolate source is a better choice, for reasons given below.

Dzurisin et al. (2005) assumed the deformation rate at Three Sisters was constant from the start of episode in 1996–1998 through 2003. Their InSAR results were for 1996–2001, GPS results for 2001–2003, and leveling results for 2002–2003. Sill-like magma chambers produce deformation that is dominated by vertical changes. The combined InSAR, GPS, and leveling dataset analyzed by Dzurisin et al. (2005) included large vertical changes from InSAR early in the deformation episode and relatively small horizontal changes from GPS later in the episode (post-2001). This is because, as we now know from longer time-series data, the deformation rate declined exponentially with time. In hindsight, by assuming that the deformation rate was constant and by combining early InSAR data (high vertical rate) and later GPS data (lower horizontal rate), Dzurisin et al. (2005) introduced a bias toward a sill-like source to their models. Also, Dzurisin et al. (2005) lacked an adequate model for spatially- and temporally-correlated errors in the InSAR data, which as a result might have been over-weighted relative to other datasets for modeling. The approach taken in this paper is to use the post-May 2001 campaign GPS, CGPS, and leveling data to determine the best-fitting source model geometry, and calculate the corresponding volume change that best fits the early InSAR observations. Then the early InSAR results were combined with the GPS and leveling results to estimate the start of the deformation episode and to infer the total source volume change. Developing a strategy for simultaneously inverting time-dependent deformation data of all three types in a mathematically rigorous way is an important objective for future work.

The spherical point pressure source (Mogi 1958), with 4 degrees of freedom (longitude, latitude, and depth to specify the source location, and ΔP, source pressure change), was the simplest model used to fit the data

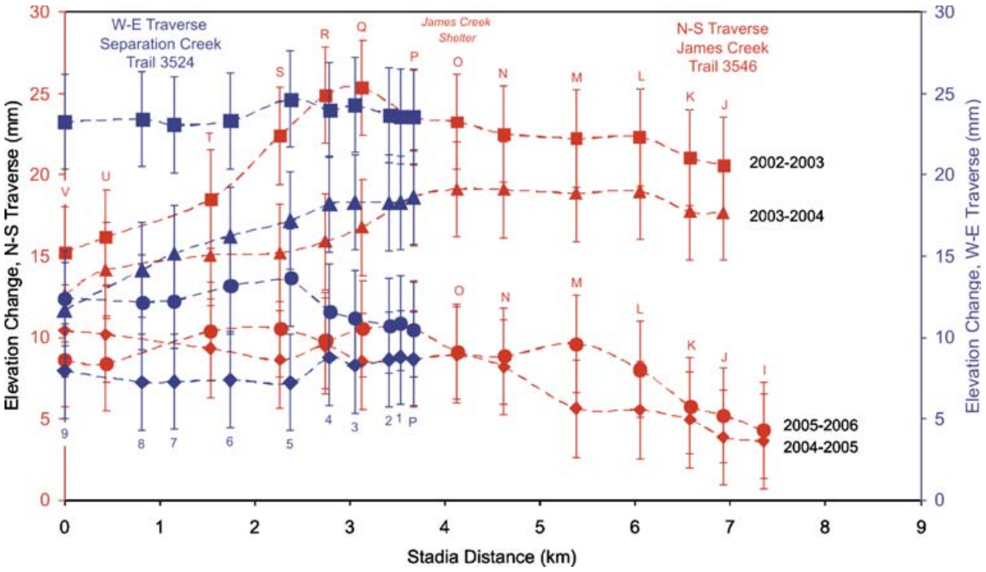

Fig. 7 Year-to-year elevation changes, August 2002–August 2006, at marks **V**–**I** and **9**–**1** from leveling surveys along N–S (red) and W–E (blue) level lines, respectively. Absolute elevation change at **V** computed from best-fit model. Level lines intersect at **P**; stadia distance for W–E line adjusted to match value at **P** with N–S line. Error bars, one standard deviation from random leveling error, random-walk mark noise with Δt=1 yr, and model uncertainty. See text for details. The signal-to-noise ratio for year-to-year elevation changes is small, so the location of maximum uplift is poorly constrained in this plot. The situation is better when the larger cumulative or net elevation changes for August 2002–August 2006 are plotted (Figs. 8 and 9, respectively). In those cases, the greatest uplift consistently occurs near marks **P** and **5** along the N–S and W–E lines, respectively

(Table 5). Assuming Poison's ratio is 0.25, a pressure increment ΔP on the inner surface of a spherical cavity with radius α (area=$4\pi\alpha^2$) will increase the cavity radius by $\Delta\alpha$, where $\Delta\alpha = \frac{1}{4}\frac{\Delta P}{G}\alpha$ (McTigue 1987). The corresponding cavity volume change is $\Delta V \cong \Delta\alpha 4\pi\alpha^2$, where G is rigidity of the host rock (we assumed a value of 30 GPa) and α is the radius of the cavity (assumed to be 1 km).

A spherical source fits the ground-based geodetic data reasonably well, i.e., with a reduced chi-square, $\chi_\nu^2 = \chi^2/(N-p)$, of 1.26, where N= 145 is the number of data and p= 4 is the model degrees of freedom. A variation of this model, which adds 3 degrees of freedom to allow for unmodeled translation of the network, improves the goodness-of-fit $\chi^2 = 159$, $\chi_\nu^2 = 1.13$. The network translation components (ΔEast, ΔNorth, ΔUp) allow for possible residual horizontal movement of the GPS network as a whole that is not accounted for by the tectonic model, for possible systematic vertical bias in the GPS data, and for

Fig. 8 Cumulative elevation-change profiles, August 2002–August 2006, at marks **V**–**I** and **9**–**1** along north-south (red) and west-east (blue) level lines, respectively. Error bars as in Fig. 7 with Δt=1–4 yr. Absolute elevation change at mark **V** computed from best-fit model

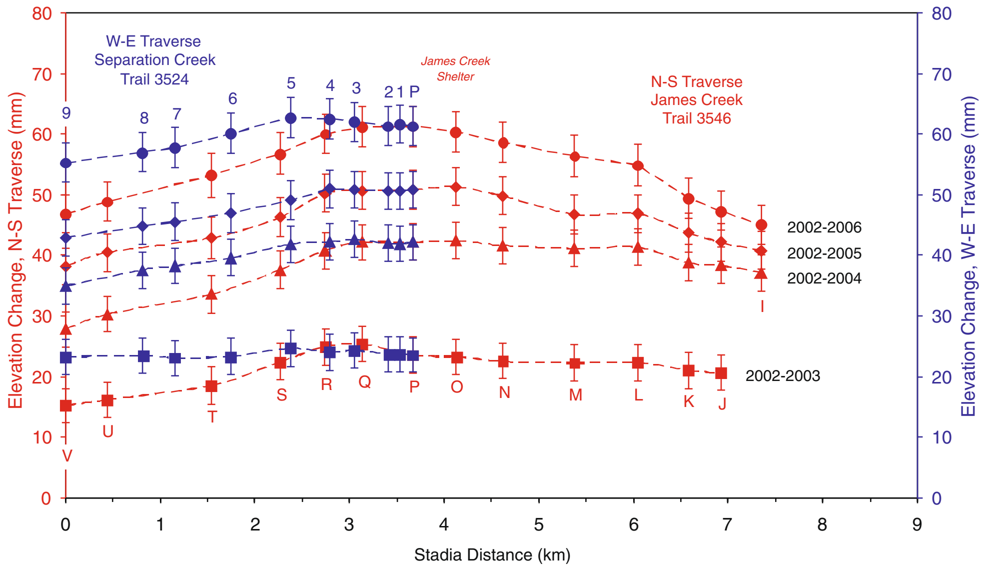

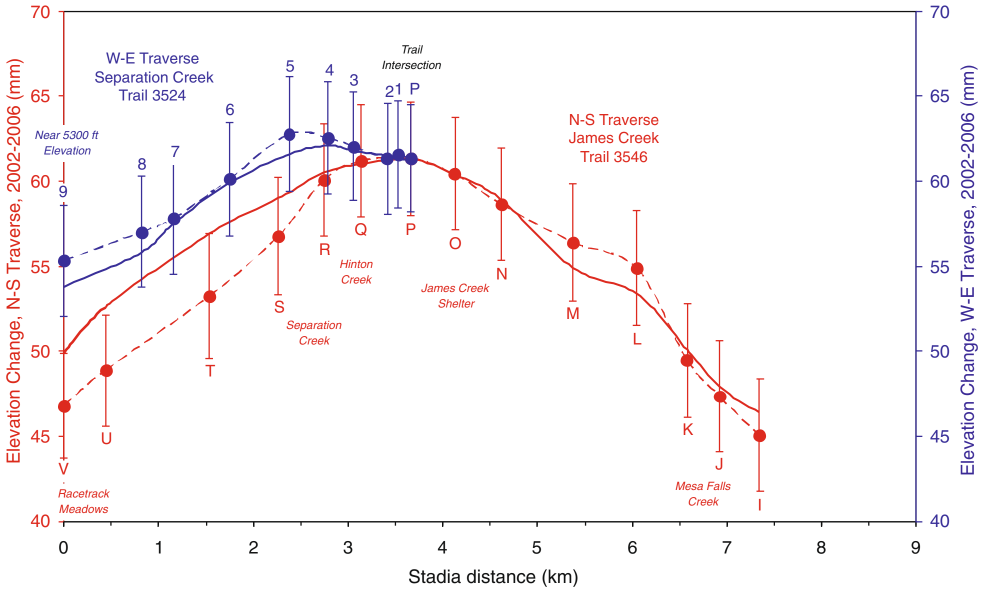

Fig. 9 Net elevation changes, August 2002–August 2006, at **V**–**I** and **9**–**1** along N–S (red) and W–E (blue) level lines, respectively. Error bars as in Fig. 7 with Δt=4 yr. Absolute elevation change at **V** computed from best-fit model. Smoothed dashed lines connect leveling observations. Solid lines represent elevation changes predicted by best-fit model (see text, **Modeling Results**) along N–S (red) and W–E (blue) lines

regional background uplift or subsidence. The network translation components are determined as free parameters in a least-squares adjustment, and the calculated components represent a network-wide correction to the observed GPS station exponential coefficients. The best-fit source depth is 5.8 km without network translation or 6.2 km with translation, where depth is relative to the mean station elevation of 1780 m.

The smaller χ^2in the model that includes a network translation is expected, because we are fitting the same data and with a more complex but similar type of model. To determine whether the improvement is statistically significant, we used the experimental F test (e.g., Gordon et al. 1987),

$$F_{calc} = \frac{\left(\chi^2_{p_1} - \chi^2_{p_2}\right) \Big/ (p_2 - p_1)}{\chi^2_{p2} \Big/ (N - P_2)} \qquad (3)$$

where $\chi^2_{p_2}$ is the misfit and p_2 is the number of free model parameters for the more complex model. If F_{calc} is greater than the upper-tailed critical value of the Fisher-Snedecor

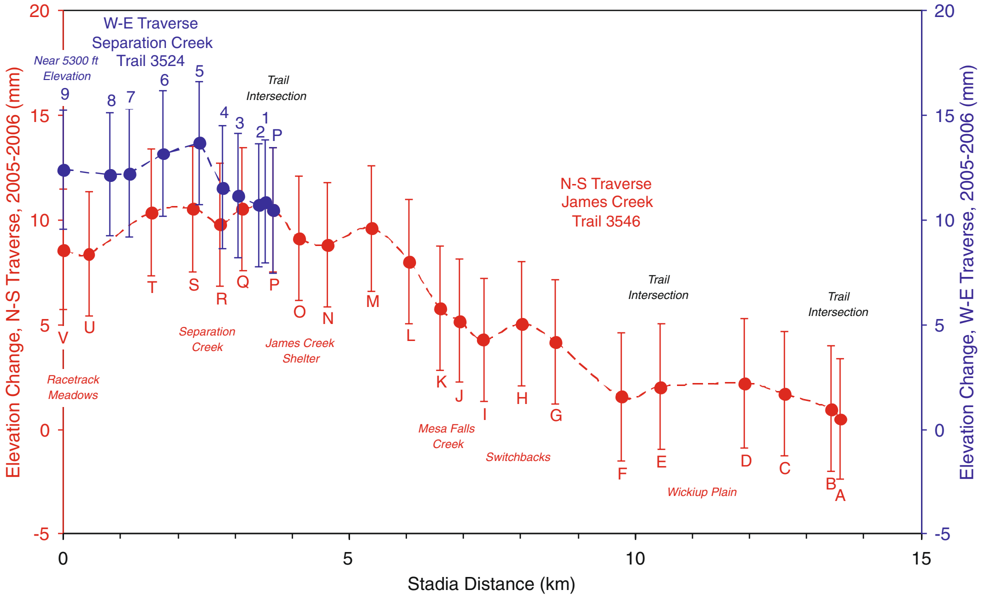

Fig. 10 Elevation changes, August 2005–August 2006, at **V**–**A** and **9**–**1** along N–S (red) and W–E (blue) level lines, respectively. Error bars as in Fig. 7 with Δt=1 yr. Absolute elevation change at **V** computed from best-fit model

Table 5 Elastic half-space deformation source models. See text for discussion

Source Description	Longitude (degree)	Latitude (degree)	Depth (km)	ΔRadius (m)	ΔEast (mm)	ΔNorth (mm)	ΔUp (mm)	Aspect Ratio	Long Axis Plunge and Trend (degree)	Degrees of Freedom	χ^2	ΔVolume (10^6 m^3)
Spherical Point Pressure (Mogi 1958)	−121.841944	44.096944	5.8	1.761 ±0.040						4	178	22.2
Spherical Point Pressure+3-D Translation	−121.841944	44.096667	6.2	2.147±0.056	1.4 ±1.6	2.3±1.6	−14.7±3.2			7	159	27.0
Vertical Prolate Spheroid	−121.838889	44.098056	4.9	2.047±0.044				0.86	90 (fixed)N/A	5	163	22.7
Vertical Prolate Spheroid+3D Translation	−121.842222	44.097500	5.4	2.356±0.061	1.6 ±1.5	1.6±1.5	−10.4±3.1	0.90	90 (fixed) N/A	8	153	26.2
Dipping Prolate Spheroid	−121.840833	44.098056	4.9	2.074±0.048				0.85	87.2 92.1	7	159	23.0
Dipping Prolate Spheroid+3D Translation	−121.840833	44.097222	5.1	±0.058	−0.4±1.5	2.3 ±1.5	−8.5±3.0	0.86	84.2 102.6	10	148	25.4

distribution $F_{p_2-p_1,N-p_2,\alpha}$, where α represents the desired rejection probability (i.e., 0.05 for 95% confidence), then the smaller $\chi^2_{p_2}$ obtained with the more complex model exceeds at a 1-α confidence limit the value that might arise from random variation in the data alone. In this case $F_{calc} = 5.5 > F_{3,138,0.05} = 2.7$, and the more complex model provides a better fit to the data with >95% confidence (Table 6). The calculated values of ΔEast and ΔNorth (1.4±1.6 mm and 2.3±1.6 mm, respectively) are small and not statistically significant, but ΔUp=−14.7±3.2 mm is relatively large. Although a spherical source with a primarily vertical network translation fits the data significantly better than a simple source, we are skeptical of the more complex model because the estimated vertical correction is near the limit of a geodetically or geologically plausible value. Note that the fit to the leveled section exponential coefficients, derived from the measured elevation changes between adjacent marks in the network, is not affected by the estimated vertical network translation.

A vertical prolate spheroid (Yang et al. 1988; Fialko and Simons 2000; Fialko et al. 2001) adds a variable aspect ratio to the source parameters, and our best-fit model of this type is both shallower (4.9 km) and stretched vertically (the aspect ratio of the horizontal to vertical semi-axis lengths=0.86) relative to the spherical source. The F test, $F_{calc} = 12.9 > F_{1,140,0.05} = 3.9$, indicates that the vertical prolate model fits better than the spherical model with >95% confidence. The more complex spherical source with a 3D translation fails to significantly improve the data fit ($F_{calc} = 1.5 < F_{2,139,0.05} = 3.1$) relative to the vertical prolate source. A prolate source will produce relatively more horizontal and less vertical deformation than a spherical source of the same power and depth. The addition of a 3-parameter network translation significantly improves the fit relative to the vertical prolate source ($F_{calc} = 3.0 > F_{3,137,0.05} = 2.7$), but this improvement again results mostly from a vertical network offset (ΔUp=−10.4±3.1 mm) that seems implausible.

Adding a variable dip and direction to the prolate spheroid source fails to significantly improve the fit relative to the simpler vertical prolate source ($F_{calc} = 1.7 > F_{2,138,0.05} = 3.1$). Nor does the corresponding dipping prolate spheroid with 3D translation significantly improve the fit relative to the simpler vertical prolate source with 3D translation ($F_{calc} = 2.4 > F_{2,135,0.05} = 3.1$).

Sill models, whether horizontal or dipping (Okada 1985; Feigl and Dupré 1999), fit the data decidedly less well than any of the models discussed here (χ^2=277 for the best-fitting dipping sill with no translation). For brevity, sill models are omitted from Table 2 and from further discussion.

We conclude that the best choice among simple elastic half space models that do not include a network translation

Table 6 Comparison of χ^2 values and of calculated and critical F-test values for model types discussed in the text. To check if a source in a given row provides a better fit to the data with 95% confidence than a source in a given column, compare the calculated and critical F-test values corresponding to that row and column. If $F_{calculated} > F_{critical}$, the source in that row provides a better fit than the source in that column. In such cases, $F_{calculated}$ is shown in square brackets. For example, all source types (rows 2–6) provide a better fit than the spherical point pressure source (column 4). Similarly, the dipping prolate spheroid fails to provide a better fit than the vertical prolate spheroid (row 3, column 5), but the vertical prolate spheroid with 3-D translation does provide a better fit than the vertical prolate spheroid (row 5, column 5). See text for discussion

Source Description	Degrees of Freedom	χ^2	Spherical Point Pressure (Mogi 1958)	Vertical Prolate Spheroid	Dipping Prolate Spheroid	Spherical Point Pressure with 3-D Translation	Vertical Prolate Spheroid with 3-D Translation
Spherical Point Pressure (Mogi 1958)	4	178.0					
Vertical Prolate Spheroid	5	162.6					
$F_{calculated}$			[12.9]				
$F_{critical}$			3.9				
Dipping Prolate Spheroid	7	159.1					
$F_{calculated}$			[5.5]	1.7			
$F_{critical}$			2.7	3.1			
Mogi with 3-D Translation	7	158.7					
$F_{calculated}$			[5.5]	1.7			
$F_{critical}$			2.7	3.1	N/A		
Vertical Prolate Spheroid with 3-D Translation	8	153.0					
$F_{calculated}$			[5.6]	[3.0]	[5.4]	[5.2]	
$F_{critical}$			2.4	2.7	3.9	3.9	
Dipping Prolate Spheroid with 3-D Translation	10	147.9					
$F_{calculated}$			[4.6]	[2.7]	[3.3]	[3.3]	2.3
$F_{critical}$			2.2	2.3	2.7	2.7	3.1

is a 4.9 km deep vertical prolate spheroid source with an aspect ratio of 0.86 (Fig. 6). If we allow for a network translation, the best choice is a 5.4 km deep vertical prolate spheroid source with an aspect ratio of 0.90 and network offsets of ΔEast=1.6±1.5 mm , ΔNorth=1.6±1.5 mm, and ΔUp=−10.4±3.1 mm. As is the case for all inverse problems of this type, the solution is non-unique if one allows for multiple sources or complicated source shapes. For example, the data could be fit arbitrarily well by a large number of shallow point sources of differing strengths. This approach could be used to simulate a shallow hydrothermal system if one were so inclined, but in our opinion such a model is not justified by the available data.

The best-fit model geometry derived from GPS and leveling data was used to estimate the source-volume change needed to reproduce the observed August 1995–August 2001 InSAR range changes, which were derived from a stack of two ERS-2 interferograms (see Fig. 1 of Dzurisin et al. 2005). Following Dzurisin et al. (2005), we sub-sampled the InSAR data using the quad-tree method (Simons et al. 2002; Jónsson et al. 2002). Next, we fit the vertical prolate spheroid source defined by the GPS and leveling data to the reduced InSAR dataset to compute a corresponding source-volume change of 23.4 x 10^6 m^3. The model predictions are compared to leveling results for August 2002–August 2006 in Fig. 9 and to InSAR results for August 1995–August 2001 in Fig. 11.

Assuming that the decay rate (b=1/5.3 $year^{-1}$) deduced from the CGPS data has remained constant throughout the episode, we estimated a start time t_0 that is consistent with both the early deformation measured with InSAR and the later deformation measured with GPS and leveling. Previously, Wicks et al. (2002), using interferograms covering different time intervals—some starting as early as 1992—concluded that the deformation episode started between August 1996 and September 1998. The total projected source volume change is equal to the sum of the August 1995–August 2001 InSAR and May 2001–August 2006 GPS + leveling modeled values, with a small correction for the 4 month overlap between the August 2001 interferogram end time and the May 2001 GPS + leveling start time. The fraction of total source-volume change during an interval is $1 - e^{-\frac{1}{5.3}(t_i - t_0)}$, where t_0 is the start of the interval and t_i the end of the interval in years. Assuming no change in source geometry, the vertical prolate source-volume changes are 23.4 x 10^6 m^3 (InSAR) and 22.7 x 10^6 m^3 (GPS + leveling, limit as $t_i \rightarrow \infty$), and the correction for the 4 month overlap is −1.25 x 10^6 m^3. The fractional source-

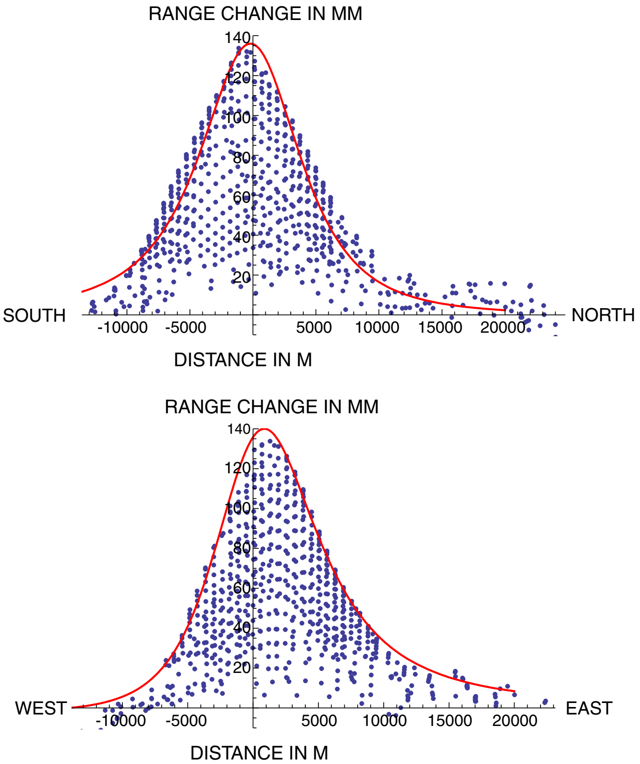

Fig. 11 Profiles of observed and modeled unwrapped, stacked InSAR range changes from August 1995 to August 2001 from Dzurisin et al. (2005). InSAR data were sub-sampled using the quad-tree method (Simons et al. 2002; Jónsson et al. 2002) and are shown in blue. Model predictions are shown in red. **Top**, InSAR data projected onto a north-south profile with the origin located directly above the source. **Bottom**, InSAR data projected onto a west-east profile. Best-fit model geometry is from the fit to GPS and leveling data. Source cavity volume change is that projected for a 1/*e* decay time of 5.3 years and a start time of September 1997. The model under-predicts the observations by less than 1 fringe (28.3 mm for ERS-2), mainly along the north-south profile. See text for discussion

volume change observed with the early InSAR is consistent with t_0=1997.8 (September 1997) as the start time of the deformation episode. In other words, the same source model that fits the GPS data for May 2001–August 2006 also fits the InSAR observations for August 1995–August 2001, assuming: (1) the inflation episode began suddenly in September 1997, and (2) the inflation rate decayed with a 1/*e* decay time of 5.3 ± 1.1 years. Agreement between the best-fit model and InSAR observations for August 1995–August 2001 is good along a west-east profile through the deformation center and acceptable along a north-south profile, where the model under-predicts the observations by less than 1 fringe (28.3 mm for ERS-2) (Fig. 11 bottom and top, respectively).

The best-fit model was used to predict vertical displacements from August 2002 to August 2006 at each of the leveling benchmarks, and those predictions were plotted together with the observed displacements for the same time period (Fig. 9). Agreement is good along the southern half of the north-south traverse (**P**–**I**) and entire west-east traverse (**9**–**1**), i.e., the model-predicted displacement profiles (solid lines) fit all of the observations (circles with error bars) within one standard deviation in the observations. Agreement between the model and observations is somewhat less good along the northern half of the north-south traverse (**V**–**P**), where the model overestimates the observed displacements by as much as 4 mm. Even so, the discrepancy is less than the uncertainty in the leveling observations at two standard deviations.

Total source-volume change from the calculated onset of inflation in September 1997 to the time of the August 2006 surveys, using a 1/*e* decay time of 5.3 years, is 36.5 x 10^6 m^3 for the best-fit vertical prolate spheroid model, or 41.9 x 10^6 m^3 for the best-fit vertical prolate spheroid model with network translation. The corresponding values at $t=\infty$, i.e., the projected volume changes for the entire episode, are 44.9 x 10^6 m^3 and 51.6 x 10^6 m^3, respectively. We estimate the uncertainty in these model volume changes to be 10–20% of the value in each case.

Discussion

The episode of surface inflation at Three Sisters that began in 1997 and was continuing at a declining rate in 2006 is suggestive of magmatic intrusion at a depth of about 5 km beneath the surface. Exponential decay in the inflation rate is consistent with: (1) a hydraulic model in which the magma flow rate from a source in the lower crust to the modeled source at ~5 km depth is proportional to the pressure difference between the two sources; or (2) sudden pressurization and subsequent time-dependent response of a viscoelastic shell (Maxwell fluid) surrounding the modeled source (e.g., high-temperature host rock surrounding a magmatic intrusion). In the hydraulic model, assuming the system is closed and elastic, magma flow from the deep source to the shallow one reduces the pressure difference in such a way that the flow rate decreases exponentially with time (Dvorak and Okamura 1987; Lu et al. 2003; Mastin et al. 2008). For the viscoelastic case, the stress induced by a sudden pressurization pulse (e.g., magmatic intrusion) causes both an instantaneous, recoverable strain and a time-dependent, permanent strain. In the latter case, the strain rate decays exponentially with a characteristic Maxwell time constant that is approximated by the ratio of the fluid strength, or viscosity, to the rigidity, or shear modulus, of the shell (Dragoni and Magnanensi 1989; Newman et al. 2001, 2006).

Another possibility is that deformation at Three Sisters is caused by injection of magmatic volatiles from a crustal magma body into an overlying hydrothermal system. Hutnak et al. (2007, 2009) ran numerical simulations of fluid flow and rock deformation in an elastic porous medium that that included multi-phase (liquid-gas) and multi-component (H_2O-CO_2) effects. They showed that, in simulations where a gas phase develops, ascent and expansion of a hot, buoyant plume can have a significant effect on the rate, magnitude, and geometry of ground surface displacements. For a plausible range of hydrologic parameters and injection rates, water and gas injection produced simulated ground surface displacement rates in the range of one to tens of mm/yr, which encompasses the rates observed at Three Sisters.

With available data, we cannot distinguish between hydraulic, viscoelastic, or poroelastic fluid-flow models for the Three Sisters uplift. This might be possible with repeated microgravity observations, which in theory could track the time history of subsurface mass change and thus distinguish among (1) ongoing intrusion at a declining rate (hydraulic model), (2) ongoing host-rock response to an intrusion that has ceased (viscoelastic model), and (3) ascent of a buoyant plume of water and gas, with attendant dilation of host rock owing to heating and gas-phase expansion (fluid-flow model). This assumes that the shape of the deformation source can be adequately constrained, and that corrections for surface height change, deformation, groundwater-level changes, magma compressibility, and other effects can be made accurately enough to resolve the remaining mass-change signal (Battaglia and Segall 2004). D.J. Johnson made repeated microgravity measurements along the N–S leveling line at Three Sisters, in conjunction with our leveling surveys, between 2002 and the time of his untimely death in October 2005. Comparison of past and future results from coordinated GPS, leveling, and gravity surveys could provide an important constraint on the mechanism(s) of surface deformation, and we recommend that such surveys be conducted for the foreseeable future.

Sporadic intrusive activity beneath Three Sisters is to be expected, given the volcanic center's recent eruptive history and geochemical evidence for an active hydrothermal system fueled by magmatic heat (Evans et al. 2004). Whether the current inflation episode will culminate in additional seismic activity, such as the swarm of ~300 small ($M_{\max}=1.9$) earthquakes that occurred in the northeast quadrant of the deforming area on March 23–26, 2004 (Dzurisin et al. 2005), is unknown. We suspect that intrusive activity in the area is sporadic with an average recurrence interval of at least several decades. Present trends indicate that an eruption in the near future is unlikely, although experience elsewhere shows that such trends can reverse suddenly. Continued vigilance is advised for both scientific and hazard-assessment purposes.

Although the deformation rate at Three Sisters has declined significantly over the past several years, the rate in 2006 was still high enough to be resolved by campaign GPS, leveling, and InSAR observations on an annual basis. Continuous GPS stations are capable of resolving the deformation signal over shorter periods, but the data are subject to spurious seasonal effects that limit their utility, especially during winter. Installation of other types of continuous deformation sensors, such as borehole tiltmeters or strainmeters, would likely not be permitted in Three Sisters Wilderness.

Autumn-to-autumn interferograms from C-band images are especially useful for defining the shape of the deformation field, but atmospheric and ionospheric phase delays typically produce anomalies as large as the current annual deformation signal (~1 fringe). Interferograms made from L-band images acquired by the Phased Array type L-band Synthetic Aperture Radar (PALSAR) aboard the Japan Aerospace Exploration Agency's Advanced Land Observing Satellite (ALOS) will be somewhat less sensitive to deformation owing to L-band's longer wavelength (23.5 cm versus 5.6 cm for C-band). However, for the same reason coherence should be much better preserved in the forested western part of the deformation field.

Leveling surveys in a remote area like the Three Sisters Wilderness pose logistical challenges. In our experience, a three-person crew camped at the James Creek shelter can cover ~3 km/day. Observing both lines in their entirely requires 5 days of surveying, which can take twice that long in typical autumn weather. The effort has been justified in this case because, on an annual basis, leveling has better sensitivity to small elevation changes than GPS or InSAR. Each technique has advantages and disadvantages, but used together they adequately characterize salient aspects of the Three Sisters deformation field. If data from CGPS stations indicate that the deformation rate is continuing to decline, the interval between future leveling and GPS surveys could be extended accordingly.

There are few documented examples of similar activity at other volcanoes with which to compare the Three Sisters case. We suspect that such episodes are common along volcanic arcs, but in the past most have gone unnoticed. Recent activity at Three Sisters differs in several respects from well-documented cases of caldera unrest that include periods of surface uplift (e.g., Yellowstone, Wyoming (Chang et al. 2007; Lowenstern et al. 2006; Puskas et al. 2007; Vasco et al. 2007); Long Valley, California (Hill et al. 2003); Phlegraean Fields, Italy (Battaglia et al. 2006); Rabaul, Papua New Guinea (McKee et al. 1995; McKee 1997)). An obvious difference is that Three Sisters is a diverse volcanic center that includes three large composite cones and numerous monogenetic basaltic vents, whereas the four examples cited above are large silicic caldera systems. In all four caldera cases, historical uplift has been episodic and interspersed with periods of quiescence or subsidence, unlike the single, monotonically declining uplift episode at Three Sisters. Surface hydrothermal activity is more muted at Three Sisters than at any of the calderas, although dilute, low-temperature springs near the center of uplift at Three Sisters have high ^{3}He/^{4}He ratios that are indicative of a magmatic source (Ingebritsen et al. 1994). The springs transport ~16 MW of heat and ~180 g/s of magmatic carbon (as CO_2) from an inferred, shallow hydrothermal system that predates the beginning of uplift (Evans et al. 2004). Another difference is that the uplift at Three Sisters is centered ~6 km west of South Sister, the nearest composite cone, and is not clearly associated with any recent vent. At each of the four calderas, on the other hand, uplift has been centrally located and mostly confined within the caldera rim; an exception is the 1995–2002 uplift at Yellowstone, which was centered along the north caldera rim and extended well outside the caldera (Wicks et al. 2006). We are not suggesting that these differences necessarily indicate different deformation mechanisms. We merely point out that such differences should be considered when comparing activity at Three Sisters to caldera unrest.

A better analog for the Three Sisters activity might be found at one or more volcanoes in the Aleutian arc, where InSAR studies have revealed numerous cases of ground deformation at relatively small volcanic centers (Lu et al. 2007). Westdahl shield volcano, for example, re-inflated following its 1991–1992 effusive eruption at an exponentially declining rate with a 1/*e* decay constant of ~6 years—similar to the 5.3 ± 1.1 years time constant for Three Sisters that we report here. Lu et al. (2000a, 2003) showed that the Westdahl behavior is consistent with a deep, constant-pressure magma source connected to a shallow reservoir by a magma-filled conduit, and proposed that the magma flow rate through the conduit is governed by the pressure gradient between the source and the reservoir. This is the hydraulic model described above; a viscoelastic model would produce similar behavior. There are some similarities between the Three Sisters uplift and that which preceded a small explosive eruption of Makushin stratovolcano in January 1995. An InSAR study showed that the eruption was preceded by ~7 cm uplift from October 1993 to September 1995 (Lu et al. 2002a). The center of uplift was offset ~5 km from the eruptive vent at Makushin, which is reminiscent of ~6 km offset between the center of uplift and the summit of South Sister. A similar ~5 km offset was observed between the center of deflation associated with the 1997 eruption of Okmok, a basaltic shield volcano, and the vent for that eruption (Lu et al. 2000b). Possible explanations for such offsets are: (1) an inclined conduit connecting a subsurface magma reservoir to a surface vent, (2) anisotropic or inelastic crustal properties resulting in an eccentric surface deformation pattern, and (3) intrusion or pressurization of a deformation source at a site unrelated to a nearby vent.

Other Aleutian examples that might be relevant to the recent activity at Three Sisters are Akutan volcano in 1996 and Mount Peulik in 1996–1998. An intense swarm of volcano-tectonic earthquakes beneath Akutan Island in March 1996 was accompanied by as much as 60 cm of uplift on the western part of the island, where Akutan volcano is located, and by a comparable amount of subsidence and extensive ground cracking on the eastern part—but no eruption. Lu et al. (2000c, 2005) modeled the surface deformation pattern as intrusion of ~0.2 km^3 of magma into a reservoir ~13 km beneath the volcano, which triggered the propagation of a magma-filled dike to within <1 km of the surface, i.e., a failed eruption. Our preferred model for uplift at Three Sisters is intrusion of a much smaller volume of magma (~0.04 km^3) at shallower depth (~5 km), which triggered the much smaller earthquake swarm in March 2004. At Three Sisters, there is no evidence of dike intrusion associated with the earthquake swarm; more likely, the seismicity indicated minor stress adjustment to ongoing inflation.

Another example of aseismic inflation (nearly so, at Three Sisters) occurred at Mount Peulik between October 1996 and September 1998. An InSAR study revealed that a presumed magma body 6.6 ± 0.5 km beneath the southwest flank of Mount Peulik inflated progressively for at least several months, resulting in a net volume increase of 0.051 ± 0.005 km^3 (Lu et al. 2002b). The inflation was not accompanied by any unusual seismicity beneath the volcano, but an intense earthquake swarm, including three magnitude 4.8–5.2 events, occurred from May to October 1998 near Becharof Lake, ~30 km northwest of Mount Peulik. Any causal relationship between the seismicity and volcano inflation is speculative, but the coincidence of the swarm and inflation episode suggest a volcano-tectonic interaction of some sort. A similar mechanism at Three Sisters seems unlikely, given the low background seismicity throughout the region, but aseismic release of tectonic strain and associated intrusive activity cannot be ruled out.

When and how the current inflation episode at Three Sisters will end is unknown. Continued seismic, geochemical, and geodetic monitoring will eventually answer such questions and hopefully provide additional insight into the cause(s) of the unrest. In the meantime, there is an opportunity to improve upon the modeling approach described here by developing a strategy for including discontinuous time-series InSAR data, with an appropriate error model, in simultaneous inversions with other geodetic datasets.

Acknowledgements Radar data used in this study were provided by the European Space Agency and Canadian Space Agency. Falk Amelung, John Langbein, William E. Scott, and an anonymous reviewer provided constructive reviews of the manuscript that led to revision and improvement of early drafts. Zhong Lu derived the relationship between vertical surface displacement and range changes observed in coeval ascending and descending interferograms. This research was supported by the USGS Volcano Hazards Program at its David A. Johnston Cascades Volcano Observatory in Vancouver, Washington, and at its Western Region Headquarters in Menlo Park, California. Use of trade names is for descriptive purposes only and does not imply endorsement by the U.S. Geological Survey.

Methods

The following material is referenced in the main body of the text and presented here for readers interested in more detailed or technical information than would be appropriate there.

1. By convention, a near-polar orbiting satellite such as Envisat, with and orbital inclination of 98.5º, travels from south to north on ascending tracks and from north to south on descending tracks. The Advanced Synthetic Aperture Radar (ASAR) aboard Envisat is right-looking, i.e., east-looking on ascending tracks and west-looking on descending tracks, with a nominal swath width of 56–105 km in various imaging modes. “Far range” refers to the eastern limit of useful backscatter data for ascending tracks and the western limit for descending tracks. During SAR processing we extended the far-range limit for images acquired on ascending track 435 beyond the usual value, which results in lower signal-to-noise and weaker coherence, especially in the eastern third of the interferogram (Fig. 2). Loss of coherence in the western ~20% of both interferograms (Figs. 1 and 2) is caused by dense forest west of the Cascade Range crest.
2. The location of maximum range change for a given deformation field differs between interferograms produced from images acquired on ascending and descending tracks, because interferograms are sensitive to both horizontal and vertical surface displacements. Relative contributions depend on the incidence angle of the SAR. For Envisat, with a relatively steep incidence angle of 19.2º–26.7º from vertical in imaging mode IS2, horizontal and vertical displacements contribute in the ratio ~1:3. In other words, Envisat interferograms are about three times more sensitive to vertical displacements than horizontal displacements. Nonetheless, horizontal displacements reinforce the effect of vertical displacements in areas where the surface moves up and toward the radar (or down and away), and diminish them where the surface moves up and away (or down and toward). For an axisymmetric deformation field such as that produced by a point or spherical source, this means that the maximum range change is shifted toward near range from the area of maximum vertical displacement. For a right-looking SAR, this corresponds to a westward shift for ascending tracks and an eastward shift for descending tracks.
3. The vertical displacement Δz at any point on the surface $p=(x, y, z)$ can be calculated from InSAR observations under the following conditions: (1) deformation interferograms that include p and span nearly the same time interval are available from both ascending and descending satellite passes, and (2) the surface displacement field is radially symmetric about point $p_0=(x_0, y_0, z_0)$, which is the surface projection of the center of the deformation source. Both conditions apply here, so: $\Delta z = \frac{(v_1 \cos\theta + v_2 \sin\theta) r_1 - (u_1 \cos\theta + u_2 \sin\theta) r_2}{(v_1 \cos\theta + v_2 \sin\theta) u_3 - (u_1 \cos\theta + u_2 \sin\theta) v_3}$, where the satellite unit look vectors (u_1, u_2, u_3) and (v_1, v_2, v_3) are in the direction (East, North, Up), θ is the azimuth at p relative to p_0 measured counterclockwise from east, and r_1 and r_2 are the range changes at p in interferograms 1 and 2, respectively. Unit look vectors for Envisat descending track 385 and ascending track 435 are given in Table 1. For a general discussion of measuring surface displacements in three dimensions using InSAR, see Wright et al. (2004).
4. Both the campaign GPS and leveling data are fit well by the same exponential decay determined from HUSB CGPS data (Table 4). Including InSAR data in a simultaneous inversion would have required either that we select a time period for which both types of data are available, or that we use the same exponential curve to calculate predicted InSAR data for input to the model. Recall that InSAR observations are available for 1992–1996, 1992–1997, 1995–1998, 1995–1999, 1996–2000, 1997–2000, 2000–2001 (Wicks et al. 2002; Dzurisin et al. 2005), and 2004–2006 (this paper). We decided that the better approach was to model the CGPS data, with a continuous time series of measurements and well documented noise model, and to compare the best-fit result to the InSAR observations.

References

Balazs EI, Young GM (1982) Corrections applied by the National Geodetic Survey to precise leveling observations. NOAA Technical Memorandum NOS NGS 34, 12 p

Battaglia M, Segall P (2004) The interpretation of gravity changes and crustal deformation in active volcanic areas. Pure Appl Geophys 161:1453–1467

Battaglia M, Troise C, Obrizzo F, Pingue F, De Natale G (2006) Evidence for fluid migration as the cause of unrest at Campi Flegrei caldera (Italy). Geophys Res Lett 33 (L01307). doi:10.1029/2005GL024904

Berardino P, Fornaro G, Lanari R, Sansosti E (2002) A new algorithm for surface deformation monitoring based on small baseline differential SAR interferograms. IEEE Trans Geosci Remote Sens 40:2375–2383

Calvert AT, Hildreth W, Fierstein J (2003) Silicic eruptions of the past 50 kyr at the Three Sisters volcanic cluster (abstract). Eos, Trans AGU, 84, Fall Meet., Suppl., Abstract V32D-1049

Chang W-L, Smith RB, Wicks C, Farrell JM, Puskas CM (2007) Accelerated uplift and magmatic intrusion of the Yellowstone caldera, 2004 to 2006. Science 318(5852):952–956. doi:10.1126/science.1146842

Dong D, Herring TA, King RW (1998) Estimating regional deformation from a combination of space and terrestrial geodetic data. J Geodesy 72:200–214

Dragoni M, Magnanensi C (1989) Displacement and stress produced by a pressurized, spherical magma chamber, surrounded by a viscoelastic shell. Phys Earth Planet Inter 56:316–328

Dvorak JJ, Okamura AT (1987) A hydraulic model to explain variations in summit tilt rate at Kilauea and Mauna Loa volcanoes. In: Decker RW, Wright TL, Stauffer PH (editors), *Volcanism in Hawaii*. US Geol Surv Prof Paper 1350:1281–1296

Dzurisin D, Lisowski L, Wicks CW, Poland MP, Endo ET (2005) Geodetic observations and modeling of magmatic inflation at the Three Sisters volcanic center, central Oregon Cascade Range, USA. J Volcanol Geotherm Res 150:35–54. doi:10.1016/j.jvolgeores.2005.07.011 The Changing Shape of Active Volcanoes

Evans WC, van Soest MC, Mariner RH, Hurwitz S, Ingebritsen SE, Wicks CW Jr, Schmidt E (2004) Magmatic intrusion west of Three Sisters, central Oregon, USA: The perspective from spring chemistry. Geology 32:69–72

Federal Geodetic Control Committee (1984) Bossler JD (chairman), Standards and specifications for geodetic control networks. National Oceanic and Atmospheric Administration, Rockville, Maryland

Feigl K, Dupré E (1999) RNGCHN: a program to calculate displacement components from dislocations in an elastic half-space with applications for modeling geodetic measurements of crustal deformation. Comp Geosci 25:695–704

Fialko Y, Simons M (2000) Deformation and seismicity in the Coso geothermal area, Inyo County, California: Observations and modeling using satellite radar interferometry. J Geophys Res 105:21–781–21,794

Fialko Y, Simons M, Khazan Y (2001) Finite source modeling of Magmatic unrest in Socorro, New Mexico, and Long Valley, California. Geophys J Int 146:191–200

Fierstein J, Calvert A, Hildreth W (2003) Two young silicic sisters at Three Sisters volcanic field, Oregon (abstract). Geological Society of America Abstracts with Programs 34(7):563

Gordon RG, Stein S, DeMets C, Argus DF (1987) Statistical tests for closure of plate motion circuits. Geophys R Lett 14(6):587–590

Hill DP, Langbein JO, Prejean S (2003) Relations between seismicity and deformation during unrest in Long Valley Caldera, California, from 1995 through 1999. J Volcan Geotherm Res 127(3–4):175–193

Hutnak M, Hurwitz S, Hsieh PA, Ingebritsen SE (2007) Numerical simulations of multi-phase, multi-component hydrothermal fluid flow: Implications for heat and mass transport and deformation of the Yellowstone Caldera. Eos Trans AGU 88 (52), Fall Meet Suppl, Abstract V51F-06

Hutnak M, Hurwitz S, Ingebritsen SE, Hsieh PA (2009) Numerical models of caldera deformation: Effects of multiphase and multicomponent hydrothermal fluid flow. J Geophys Res. 114, B04411. doi:10.1029/2008JB006151

Ingebritsen SE, Mariner RH, Sherrod DR (1994). Hydrothermal systems of the Cascade Range, north-central Oregon. US Geol Surv Prof Pap 1044-L, 86 p

Jónsson S, Zebker H, Segall P, Amelung F (2002) Fault slip distribution of the 1999 M_w 7.1 Hector Mine, California, earthquake, estimated from satellite radar and GPS measurements. Bull Seism Soc Am 92:1377–1389

Langbein J (2004) Two-color electronic distance meter measurements revisited. J Geophys Res, 109 B04406. doi:10.1029/2003JB002819

Langbein J (2008) Noise in GPS displacement measurements from Southern California and Southern Nevada, J Geophys Res, 113 B04406. doi:10.1029/2007JB005247

Lohman R and Simons M (2005) Some thoughts on the use of InSAR data to constrain models of surface deformation: noise structure and data downsampling. Geochem Geophys Geosyst 6. doi:10.1029/2004GC000841

Lowenstern JB, Smith RB, Hill DP (2006) Monitoring super-volcanoes: geophysical and geochemical signals at Yellowstone and other caldera systems. Philos Trans R Soc 264(1845):2055–2072

Lu Z, Wicks C Jr, Dzurisin D, Thatcher W (2000a) Aseismic inflation of Westdahl volcano, Alaska, revealed by satellite radar interferometry. Geophys Res Lett 27(11):1567–1570

Lu Z, Mann D, Freymueller J, Meyer D (2000b) Synthetic aperture radar interferometry of Okmok volcano, Alaska: Radar observations. J Geophys Res 105:10 791–10,806

Lu Z, Wicks C Jr, Power JA, Dzurisin D (2000c) Ground deformation associated with the March 1996 earthquake swarm at Akutan volcano, Alaska, revealed by satellite radar interferometry. J Geophys Res 105(B9):21 ,483–21,495

Lu Z, Power JA, McConnell VS, Wicks C, Dzurisin D (2002a) Preeruptive inflation and surface interferometric coherence characteristics revealed by satellite radar interferometry at Makushin Volcano, Alaska: 1993–2000. J Geophys Res 107 (B11):2266. doi:10.1029/2001JB000970

Lu Z, Wicks C Jr, Dzurisin D, Power JA, Moran SC, Thatcher W (2002b) Magmatic inflation at a dormant stratovolcano: 1996–1998 activity at Mount Peulik volcano, Alaska, revealed by satellite radar interferometry. J Geophys Res 107 (B7). doi:10.1029/2001/JB000471

Lu Z, Masterlark T, Dzurisin D, Rykhus R, Wicks C Jr (2003) Magma supply dynamics at Westdahl Volcano, Alaska, modeled from satellite radar interferometry. J Geophys Res 108(B7):2354. doi:10.1029/2002JB002311

Lu Z, Wicks C Jr, Kwoun O, Power J, Dzurisin D (2005) Surface deformation associated with the March 1996 earthquake swarm at Akutan Island, Alaska, revealed by C-band ERS and L-band JERS radar interferometry. Can J Remote Sens 31(1):7–20

Lu Z, Dzurisin D, Wicks C Jr, Power J, Kwoun O, Rykhus R (2007) Diverse deformation patterns of Aleutian volcanoes from satellite interferometric synthetic aperture radar (InSAR). In: Eichelberger, J.C., Gordeev, E., Izbekov, P., Kasahara, M., and Lees, J.M. (editors), *Volcanism and Subduction*, AGU Monograph Series 172:249–261. doi:10.1029/172GM18

Mastin LG, Roeloffs Evelyn, Beeler NM, Quick JE (2008) Constraints on the size, overpressure, and volatile content of the Mount St. Helens magma system from geodetic and dome-growth measurements during the 2004–2006+ eruption. Chap. 22 *in* Sherrod DR, Scott WE, Stauffer PH (eds), A volcano rekindled: the renewed eruption of Mount St. Helens, 2004–2006. US Geological Survey Professional Paper 1750, 856 p and DVD-ROM

McCaffrey RM, Long MD, Goldfinger C, Zwick PC, Nableck JL, Johnson CK, Smith C (2000) Rotation and plate locking at the southern Cascadia subduction zone. Geophys Res Lett 27:3117–3120

McCaffrey R, Qamar AI, King RW, Wells R, Khazaradze G, Williams CA, Stevens CW, Vollick JJ, Zwick PC (2007) Fault locking, block rotation and crustal deformation in the Pacific Northwest. Geophys J Int . doi:10.1111/j.1365-246X.2007.03371.x

McKee CO (1997) Lessons from unrest and eruption at Rabaul. In: Program and Abstract 2nd Merapi Decade Volcano International Workshop, Volcanological Survey of Indonesia and UNESCO, 36

McKee C, Talai B, Lauer N, Stewart R, de Saint Ours P, Itikarai I, Patia H, Lolok D, Davies H, Johnson RW (1995). The 1994 eruptions at Rabaul Volcano, Papua New Guinea. International

Union of Geodesy and Geophysics, General Assembly, 21, Week A, 448

McTigue DF (1987) Elastic stress and deformation near a finite spherical magma body: resolution of the point source paradox. J. Geophys. Res. 92:12,931–12,940.

Mogi K (1958) Relations between the eruptions of various volcanoes and the deformation of the ground surfaces around them. Bull Earthq Res Inst U Tokyo 36:99–134

Newman AV, Dixon TH, Ofoegbu G, Dixon JE (2001) Geodetic and seismic constraints on recent activity at Long Valley caldera, California: Evidence for viscoelastic rheology. J Volcan Geoth Res 105:183–206

Newman AV, Dixon TH, Gourmelen N (2006) A four-dimensional viscoelastic deformation model for Long Valley Caldera, California, between 1995 and 2000. J Volcan Geoth Res 150:244–269. doi:10.1016/j.jvolgeores.2005.07.017

Okada Y (1985) Surface deformation due to shear and tensile faults in a half-space. Bull Seismol Soc Am 75:1135–1154

Puskas C, Smith RB, Meertens CM, Chang WL (2007) Crustal deformation of the Yellowstone–Snake River Plain volcano-tectonic system; campaign and continuous GPS observations, 1987–2004. J Geophys Res 112 (B03401), doi:10.1029/2006JB004325

Savage JC, Svarc JL, Prescott, WH (2001a) Strain accumulation near Yucca Mountain, Nevada, 1993–1998. J Geophys Res 106:16,483–16,488

Savage JC, Gan W, Svarc JL (2001b) Strain accumulation in the Eastern California Shear Zone. J Geophys Res 106 (B10):21, 995–22,007

Scott WE (1987) Holocene rhyodacite eruptions on the flanks of South Sister volcano, Oregon. In: Fink JH (editor), *The Emplacement of Silicic Domes and Lava Flows*. Geol Soc Am Spec Pap 212:35–53

Scott WE, Iverson RM, Schilling SP, Fischer BJ (2001) Volcano hazards in the Three Sisters region, Oregon. US Geol Surv Open-File Report 99-437, 14 p

Sherrod DR, Taylor EM, Ferns ML, Scott WE, Conrey RM, Smith GA (2004) Geologic map of the Bend 30- by 60-minute quadrangle, central Oregon. US Geological Survey Miscellaneous Field Investigations Map , I-2683, scale 1:100,000 scale, 48-page pamphlet

Simons M, Fialko Y, Rivera L (2002) Coseismic deformation from the 1999 M_w 7.1 Hector Mine, California, earthquake, as inferred from InSAR and GPS observations. Bull Seism Soc Am 92:1390–1402

Svarc JL, Savage JC, Prescott WH, Murray MH (2002) Strain accumulation and rotation in western Oregon and southwestern Washington. J Geophys Res 107. doi:10.1029/2001/JB000625

Vanicek P, Castle RO, Balazs EI (1980) Geodetic leveling and its applications. Rev Geophys:18, 505–524

Vasco DW, Puskas CM, Smith RB, Meertens CM (2007) Crustal deformation and source models of the Yellowstone volcanic field from geodetic data. J Geophys Res 112 (B03401). doi:10.1029/2006JB004325

Wicks CW Jr, Dzurisin D, Ingebritsen S, Thatcher W, Lu Z, Iverson J (2002) Magmatic activity beneath the quiescent Three Sisters volcanic center, central Oregon Cascade Range, USA. Geophys Res Lett 29 (7):26-1–26-4

Wicks C, Thatcher W, Dzurisin D, Svarc J (2006) Uplift, thermal unrest, and magma intrusion at Yellowstone caldera. Nature 440:72–75

Williams SD, Bock Y, Fang P, Jamason P, Nikolaidis RM, Prawirodirdjo L, Miller M, Johnson DJ (2004) Error analysis of continuous GPS position time series. J Geophys Res 109 (B03412). doi:10.1029/2003JB00274

Wright T J, Parsons BE, Lu Z (2004) Toward mapping surface deformation in three dimensions using InSAR, Geophys Res Lett 31 (L01607). doi:10.1029/2003GL018827

Wyatt FW (1989) Displacement of surface monuments: Vertical motion. J Geophys Res 94:1655–1664

Yang X-M, Davis PM, Dietrich JH (1988) Deformation from inflation of a dipping finite prolate spheroid in an elastic half-space as a model for volcanic stressing. J Geophys Res 93:4249–4257

Zumberge JF, Heflin MB, Jefferson DC, Watkins MM, Webb FH (1997) Precise point positioning for the efficient and robust analysis of GPS data from large networks. J Geophys Res 102 (B3):5005–5017